

Oxygen-evolving photosystem II structures during S_1 – S_2 – S_3 transitions

<https://doi.org/10.1038/s41586-023-06987-5>

Received: 29 June 2023

Accepted: 15 December 2023

Published online: 31 January 2024

Open access

 Check for updates

Hongjie Li^{1,12}, Yoshiki Nakajima^{1,12}, Eriko Nango^{2,3}, Shigeki Owada⁴, Daichi Yamada⁵, Kana Hashimoto¹, Fangjia Luo⁴, Rie Tanaka^{3,6}, Fusamichi Akita¹, Koji Kato¹, Jungmin Kang³, Yasunori Saitoh¹, Shunpei Kishi¹, Huaxin Yu¹, Naoki Matsubara¹, Hajime Fujii¹, Michihiro Sugahara⁴, Mamoru Suzuki⁷, Tetsuya Masuda⁸, Tetsunari Kimura⁹, Tran Nguyen Thao¹, Shinichiro Yonekura¹, Long-Jiang Yu^{1,10}, Takehiko Toshi³, Kensuke Tono⁴, Yasumasa Joti⁴, Takaki Hatsui⁴, Makina Yabashi⁴, Minoru Kubo⁵, So Iwata^{3,6}, Hiroshi Isobe¹, Kizashi Yamaguchi¹¹, Michihiro Suga^{1,12}✉ & Jian-Ren Shen¹✉

Photosystem II (PSII) catalyses the oxidation of water through a four-step cycle of S_i states ($i = 0-4$) at the Mn_4CaO_5 cluster¹⁻³, during which an extra oxygen (O6) is incorporated at the S_3 state to form a possible dioxygen⁴⁻⁷. Structural changes of the metal cluster and its environment during the S-state transitions have been studied on the microsecond timescale. Here we use pump-probe serial femtosecond crystallography to reveal the structural dynamics of PSII from nanoseconds to milliseconds after illumination with one flash (1F) or two flashes (2F). Y_Z , a tyrosine residue that connects the reaction centre P680 and the Mn_4CaO_5 cluster, showed structural changes on a nanosecond timescale, as did its surrounding amino acid residues and water molecules, reflecting the fast transfer of electrons and protons after flash illumination. Notably, one water molecule emerged in the vicinity of Glu189 of the D1 subunit of PSII (D1-E189), and was bound to the Ca^{2+} ion on a sub-microsecond timescale after 2F illumination. This water molecule disappeared later with the concomitant increase of O6, suggesting that it is the origin of O6. We also observed concerted movements of water molecules in the O1, O4 and Cl-1 channels and their surrounding amino acid residues to complete the sequence of electron transfer, proton release and substrate water delivery. These results provide crucial insights into the structural dynamics of PSII during S-state transitions as well as O–O bond formation.

Photosystem II (PSII) produces dioxygen by extracting electrons and protons from water, which takes place at the oxygen-evolving complex (OEC), an oxo-bridged Mn_4CaO_5 cluster with a shape that resembles a distorted chair^{2,3,8}. The Mn atoms in the OEC accumulate oxidative power through a four-step cycle of S_i states ($i = 0-4$) that is initiated by the light-driven excitation of P680, a reaction centre that is a complex of chlorophyll *a* molecules¹ (Extended Data Fig. 1a)¹. This is followed by a rapid charge separation that produces a pair of positive and negative charges on P680⁺/pheophytin⁻ (Pheo⁻) on a picosecond timescale^{9,10}. The electron is transferred from Pheo⁻ to the primary and secondary plastoquinones Q_A and Q_B (Extended Data Fig. 1b). The P680⁺ is then reduced by a tyrosine residue (D1-Y161; Y_Z) located between P680 and the OEC, which is re-reduced by the OEC, pushing the OEC to a higher S_i state¹¹. In conjunction with the oxidation of the OEC, protons are released in a 1:0:1:2 stoichiometry for the S_0 – S_1 , S_1 – S_2 , S_2 – S_3 and S_3 –(S_4)– S_0 transitions¹²⁻¹⁴, and two water molecules are split to produce a

dioxygen in the S_3 –(S_4)– S_0 transition, after which the OEC returns to its most reduced S_0 state.

The water-splitting reaction requires a constant replenishment of water from the lumen, as well as the prompt elimination of the generated protons into the lumen. There are extensive hydrogen-bonding networks connecting the OEC with the lumen, and among these, the O1, O4 and Cl-1 channels are proposed to have essential roles in the water-splitting reaction^{6,15-18} (Extended Data Fig. 1c). (Note that the first 56 water molecules are named following a previous report¹⁸, and other water molecules are newly numbered; see Supplementary Table 1 for corresponding numbers in other studies). The O1 channel is a wide channel starting from a five-water cluster (W10, W20, W21, W22 and W23) that is located near O1 of the OEC (OEC-O1). This channel travels across a narrow area and ends at a giant cavity in which two glycerol molecules are found in the crystal structure^{2,3} (Extended Data Fig. 1c). The wide O1 channel might give a high mobility of water within it, and is

¹Research Institute for Interdisciplinary Science, Graduate School of Natural Science and Technology, Okayama University, Okayama, Japan. ²Institute of Multidisciplinary Research for Advanced Materials, Tohoku University, Sendai, Japan. ³RIKEN SPring-8 Center, Sayo, Japan. ⁴Japan Synchrotron Radiation Research Institute, Sayo, Japan. ⁵Department of Picobiology, Graduate School of Life Science, University of Hyogo, Kobe, Japan. ⁶Department of Cell Biology, Graduate School of Medicine, Kyoto University, Kyoto, Japan. ⁷Institute for Protein Research, Osaka University, Osaka, Japan. ⁸Division of Food and Nutrition, Faculty of Agriculture, Ryukoku University, Otsu, Japan. ⁹Department of Chemistry, Graduate School of Science, Kobe University, Kobe, Japan.

¹⁰Key Laboratory of Photobiology, Institute of Botany, Chinese Academy of Sciences, Beijing, China. ¹¹Center for Quantum Information and Quantum Biology, Osaka University, Osaka, Japan.

¹²These authors contributed equally: Hongjie Li, Yoshiki Nakajima. ✉e-mail: michisuga@okayama-u.ac.jp; shen@okayama-u.ac.jp

therefore considered as a potential water inlet pathway^{6,17}. By contrast, the O4 channel is a shorter channel that starts at OEC-O4 and ends at a four- or five-water cluster (Extended Data Fig. 1c). The CI-1 channel refers to a hydrogen-bonding network mediated by CI-1, which spans from W1 to W4, continues through D1-D61 and further extends to an ionic gate comprising D1-E65, D1-R334 and D2-E312 (Extended Data Fig. 1c). Cl⁻ ions are essential for the progression of PSII beyond the S₂ state^{19–21}, and the CI-1 channel is thought to serve as a proton-release pathway in the S₂–S₃ transition^{17,22,23}.

Pump-probe time-resolved femtosecond crystallography (TR-SFX) has provided a lot of information about the intermediate S-state structures of PSII (refs. 4–7,17,24,25). However, time-resolved structures at shorter timescales during the S₁–S₂ and S₂–S₃ transitions are lacking, and thus the sequence of OEC oxidation, proton release, electron transfer and water delivery before O6 incorporation is unclear. Here we investigate the structural dynamics during the S₁–S₂ and S₂–S₃ transitions using the pump-probe TR-SFX method at delay times (Δt) of 20 ns to 5 ms (Extended Data Fig. 1d). We identify structural changes associated with electron transfer, proton release and water delivery at various regions, including Q_A–Q_B, Y_Z, the OEC and the O1, O4 and CI-1 channels. Notably, we observe the presence of a water molecule close to Ca at initial stages of the S₂–S₃ transition. This water molecule subsequently disappears with the concomitant increase of the O6 electron density, suggesting that it is the origin of O6. Our findings provide spatial and time-resolved snapshots of the S₁–S₂–S₃ state transitions, which are important for the mechanism of O–O bond formation.

Data quality

We obtained 14 datasets at resolutions ranging from 2.15 to 2.30 Å, with redundancy values higher than 100 even at the highest-resolution shells, after 1F or 2F (Extended Data Table 1). For all datasets, we calculated the $F_{\text{obs}}(1F(\Delta t1)) - F_{\text{obs}}(\text{Dark})$ and $F_{\text{obs}}(2F(\Delta t2)) - F_{\text{obs}}(1F)$ isomorphous-difference density maps at 2.3-Å resolution. The R_{iso} values between the intermediate and ground states ranged from 6% to 11% (Supplementary Table 2)—sufficiently low to allow the confident detection of subtle structural changes during S_i-state transitions. We observed substantial difference densities in the Q_A–Q_B and OEC regions and in the proton and water channels at the electron donor side; their intensities are listed in Supplementary Table 3.

Structural changes in the Q_A–Fe–Q_B area

Q_A and Q_B are linked to the non-haem iron through hydrogen bonds with D2-H214 and D1-H215, forming an iron–quinone complex. The carbonyl oxygens of the Q_A and Q_B heads are also hydrogen-bonded to D2-F261 and to D1-F265/D1-S264, respectively (Fig. 1).

Large difference densities appear on the Q_A side at $\Delta t1 = 20$ ns and $\Delta t1 = 200$ ns, become weak at $\Delta t1 = 1 \mu\text{s}$ to $\Delta t1 = 200 \mu\text{s}$ and vanish at $\Delta t1 = 5$ ms (Fig. 1a and Supplementary Video 1). These changes correspond to the formation of Q_A⁻, the oxidation of Q_A⁻ to Q_A and the completion of Q_A⁻ oxidation, respectively. The formation of Q_A⁻ causes the counterclockwise rotation of its head group, concomitant with similar rotations or movements of D2-F261, D2-W253 and D2-H214, which surround Q_A (Fig. 1a and Supplementary Video 1). The formation of Q_A⁻ also induces a shift of the non-haem iron by about 0.2 Å towards Q_A. The pair of positive and negative difference densities around the non-haem iron is strongest at $\Delta t1 = 20$ ns and $\Delta t1 = 200$ ns, which is much faster than the time needed for the reduction of Fe³⁺ by Q_A⁻ (7 μs in refs. 26,27), indicating that the movement of the non-haem iron is caused not by its reduction but rather by the attraction of electropositive Fe³⁺ to Q_A⁻. The diminishing difference densities around Q_A and the non-haem iron at $\Delta t1 = 1 \mu\text{s}$ to $\Delta t1 = 200 \mu\text{s}$ suggest that the attraction between the non-haem iron and Q_A⁻ is decreased and that the electron on Q_A⁻ is transferred to the non-haem iron (Fig. 1a and Supplementary Video 1).

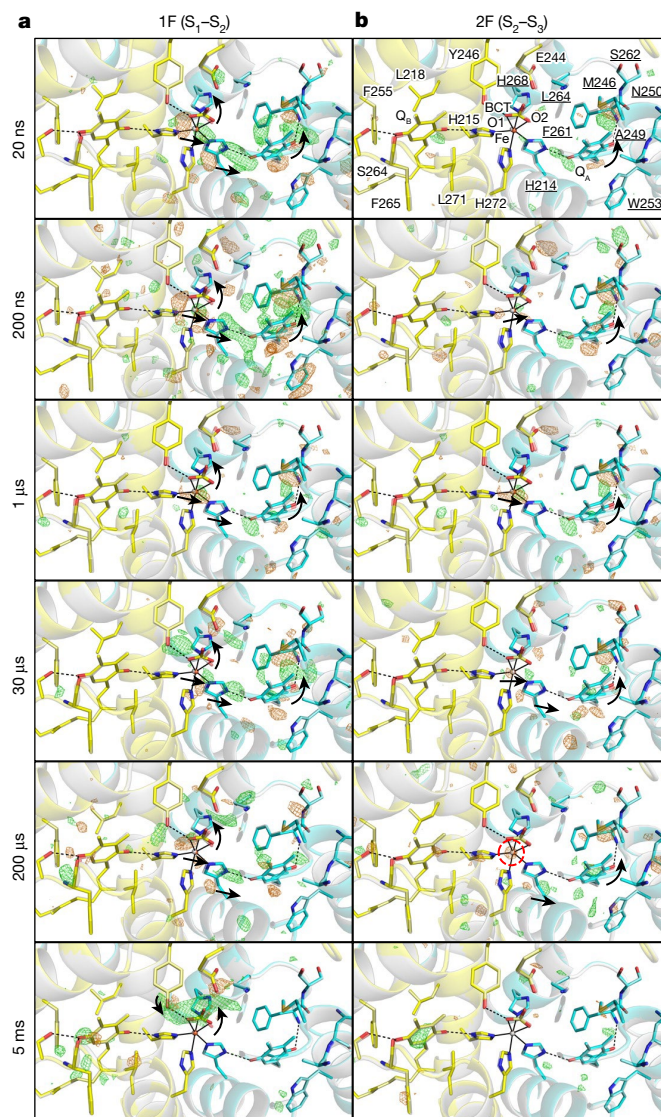


Fig. 1 | Structural dynamics in the Q_A–Q_B area during S₁–S₂–S₃ transitions. **a, b.** Structures of PSII in the Q_A–Q_B area are superposed with $F_{\text{obs}}(1F) - F_{\text{obs}}(\text{Dark})$ (**a**) and $F_{\text{obs}}(2F) - F_{\text{obs}}(1F)$ (**b**) difference density maps contoured at $+3.5\sigma$ (green) and -3.5σ (orange) from 20 ns to 5 ms. Ground-state models (dark in **a** and 1F in **b**) are depicted in grey, and the D1 and D2 proteins in the intermediate structures are shown in yellow and cyan, respectively. Residues of D1 and D2 are depicted without and with underlines, respectively. Hydrogen bonds are shown by black dotted lines. Black solid lines link the cofactors in PSII and their ligands. Black arrows indicate structural changes based on the refined models. The ordered and disordered atoms (non-haem iron in this figure and water molecules in the other figures) in the intermediate structures are encircled by cyan- and red-dotted lines, respectively. These nomenclature, hydrogen bonds, ligands of cofactors and black arrows are used in the other figures, unless otherwise stated.

By $\Delta t1 = 5$ ms, these difference densities disappear entirely, indicating the completion of the electron transfer together with the restoration of Q_A and the non-haem iron.

The distances from two carbonyl oxygens of bicarbonate (BCT; BCT-O1 and BCT-O2) to the non-haem iron increase from 2.16 Å and 2.28 Å in the dark state to 2.43 Å and 2.44 Å after 5 ms of 1F (Fig. 1a, Extended Data Table 2 and Supplementary Video 1). These increases most likely reflect changes in the binding environment of BCT owing to the reduction of the non-haem iron. At $\Delta t1 = 5$ ms, a large positive difference density appears between BCT and D1-Y246 (Fig. 1a and Supplementary Video 1), consistent with our previous discovery²⁵, and

the distance between D1-Y246 and BCT-O1 decreases from 3.21 Å to 2.82 Å. At $\Delta t_1 = 200 \mu\text{s}$ to $\Delta t_1 = 5 \text{ms}$, the Q_B head shifts slightly, which might be a result of the movement of BCT or the partial reduction of Q_B by Q_A^- (ref. 28).

From $\Delta t_2 = 20 \text{ns}$ to $\Delta t_2 = 30 \mu\text{s}$, the Q_A head rotated in a counter-clockwise direction, and this was accompanied by a movement of the non-haem iron towards Q_A^- —structural changes similar to those observed after 1F. However, the difference densities associated with these structural changes were much weaker after 2F (Fig. 1 and Supplementary Video 2). The non-haem iron remains Fe^{2+} at 5 ms after photoreduction by 1F, because its re-oxidation by ferricyanide takes 20 s (ref. 27) (Extended Data Fig. 1d). For this reason, the electron of Q_A^- does not travel to the non-haem iron, but rather travels directly to Q_B after 2F, resulting in the absence of difference density on BCT and the appearance of positive difference density on the Q_B head at $\Delta t_2 = 5 \text{ms}$ (ref. 4) (Fig. 1b and Supplementary Video 2). The non-haem iron becomes disordered at $\Delta t_2 = 200 \mu\text{s}$ but ordered by $\Delta t_2 = 5 \text{ms}$, which is presumably related to electron transfer from Q_A^- to Q_B during this time.

Structural changes around Y_Z

D1-V157, D1-F186, D1-I192 and D1-I290 lie between Y_Z and P_{D1} (P680 at the D1 side) (Extended Data Figs. 1b and 2), and Y_Z is connected to the O1 channel through W4 and D1-Q165, to the Cl-I channel through W7 and to the OEC through W3, W4 and W7 (Extended Data Fig. 1c). Y_Z forms a short (low-barrier) hydrogen bond with D1-H190 (2.44 Å in the Protein Data Bank (PDB) under accession code 3WU2; ref. 2), through which the phenolic proton of Y_Z^{+} migrates to D1-H190, forming Y_Z^- -D1-H190 $^+$ during the S_1 - S_2 state transitions^{11,29–31}. At $\Delta t_1 = 20 \text{ns}$, two negative difference densities first appear adjacent to D1-Q165 and Y_Z , and at $\Delta t_1 = 200 \text{ns}$, pairs of positive and negative difference densities appear over D1-Q165, Y_Z and D1-F186, indicating their correlated movements towards P680 (Fig. 2a and Extended Data Fig. 2a,b). These movements might be in preparation for the subsequent electron transfer from Y_Z to P680. Simultaneously with these movements, a positive difference density appears on the Mg atom of P_{D1} (Fig. 2a and Supplementary Table 3), which might reflect the re-reduction of $P680^+$ by Y_Z .

D1-H190 moves away from Y_Z at $\Delta t_1 = 200 \text{ns}$, which, together with the movement of Y_Z toward P680, causes the elongation of the hydrogen bond between Y_Z and D1-H190 from 2.51 Å to 2.80 Å at $\Delta t_1 = 200 \text{ns}$ (Fig. 2a, Extended Data Fig. 3 and Supplementary Video 3). These changes suggest that Y_Z is first oxidized by $P680^+$ and subsequently deprotonated, forming a Y_Z^- /D1-H190 $^+$ species, with the time constant of Y_Z oxidation consistent with that reported for $P680^+$ reduction in the S_1 - S_2 transition^{31,32}. At $\Delta t_1 = 1 \mu\text{s}$ and $\Delta t_1 = 30 \mu\text{s}$, difference densities on D1-Q165, Y_Z and D1-H190 decrease, indicating that they have moved to their original locations. In addition, a strong negative difference density appears on W7, suggesting that W7 is disordered during this period (Fig. 2a and Supplementary Video 3). By $\Delta t_1 = 200 \mu\text{s}$, all difference densities vanish at the Y_Z area, indicating the restoration of all residues and water, and the Y_Z -D1-H190 distance returns to 2.53 Å (Fig. 2a, Extended Data Fig. 3, Extended Data Table 2 and Supplementary Video 3). The trajectories of the Y_Z area at $\Delta t_1 = 1 \mu\text{s}$ and $\Delta t_1 = 30 \mu\text{s}$ correspond to the re-reduction and re-protonation of Y_Z^- to Y_Z , which completes by $\Delta t_1 = 200 \mu\text{s}$, consistent with the 55–85- μs half-life of Y_Z^{+} re-reduction by the OEC in the S_1 - S_2 transition^{33,34}.

After 2F, difference densities start to appear only after $\Delta t_2 = 200 \text{ns}$ (Fig. 2b and Supplementary Movie 4). These lagged difference densities likely correspond to the slower and biphasic 50-ns and 280-ns components of the $P680^+$ decay in the S_2 - S_3 transition^{31,32}. This delay might arise from the reduced rate of electron transfer to $P680^+$ owing to the accumulation of a positive charge on the OEC. Difference densities on Y_Z and D1-Q165 increase at $\Delta t_2 = 1 \mu\text{s}$, and the Y_Z -D1-H190 distance increases slightly from $\Delta t_2 = 0$ to $\Delta t_2 = 1 \mu\text{s}$ (Extended Data Fig. 3, Extended Data Table 2 and Supplementary Video 4). These

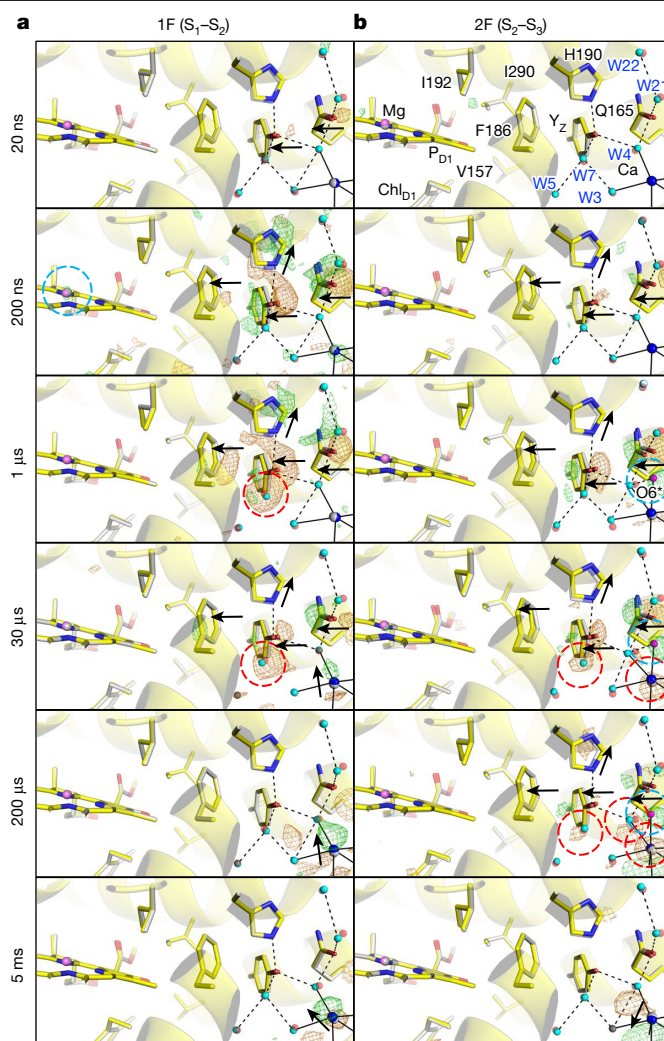


Fig. 2 | Structural dynamics in the Y_Z area during S_1 - S_2 - S_3 transitions.

a, b, Structures of PSII in the Y_Z area are superposed with $F_{\text{obs}}(1F) - F_{\text{obs}}(\text{Dark})$ (**a**) and $F_{\text{obs}}(2F) - F_{\text{obs}}(1F)$ (**b**) difference density maps contoured at $+4.0\sigma$ (green) and -4.0σ (orange), with delay times from 20 ns to 5 ms. Water molecules at ground and intermediate states are depicted by red and cyan spheres, respectively. The Mg atom in P_{D1} is shown as a grey sphere for the ground structure and a violet sphere for the intermediate structure. $O6^*$ and $O6$ (in the other figures) are depicted in magenta, and the Ca ion of the OEC is in blue. The same colour scheme is used in other figures, unless otherwise stated.

findings suggest the oxidation of Y_Z and a potential proton transfer from Y_Z to D1-H190 at $\Delta t_2 = 1 \mu\text{s}$, which is similar to that observed at $\Delta t_1 = 20 \text{ns}$ – 200ns . At $\Delta t_2 = 30 \mu\text{s}$, difference densities on Y_Z and D1-Q165 decrease, indicating the re-reduction of Y_Z^- by the OEC. The difference density on Y_Z becomes even weaker at $\Delta t_2 = 200 \mu\text{s}$, but is still present (Fig. 2b and Supplementary Video 4), indicating that the reduction of Y_Z is not yet complete, which is compatible with the half-life of 140–90 μs of Y_Z reduction^{33,34}. Y_Z reduction is completed by 5 ms, and difference densities disappear at the Y_Z area and all residues and water molecules are restored (Fig. 2b and Supplementary Video 4). The time-resolved redox states of Y_Z after 1F and 2F that are described above are summarized in Extended Data Fig. 2c.

Oxidation of the OEC during the S_1 - S_2 transition

Notable positive difference densities first appear on Mn4 and subsequently cover all four Mn and one Ca ions at $\Delta t_1 = 20 \text{ns}$ – 200ns before OEC oxidation (Fig. 3a and Supplementary Video 3). Nevertheless,

metal–metal distances remain largely unchanged (Extended Data Fig. 3 and Extended Data Table 2), suggesting a possible charge rearrangement on the OEC triggered by the electrostatic effect of the oxidized Y_Z^{+}/Y_Z . At $\Delta t_1 = 1 \mu\text{s}$, difference densities on Mn1–Mn3 and Ca vanish, whereas that on Mn4 continues (Fig. 3a and Supplementary Video 3). At $\Delta t_1 = 30 \mu\text{s}$, paired negative and positive difference densities appear on two sides of Ca, indicating that Mn4 and Ca move outwards from the OEC, causing an increase in the Mn4–Ca distance from 3.83 Å at $\Delta t_1 = 200 \text{ ns}$ to 3.96 Å at $\Delta t_1 = 30 \mu\text{s}$. By $\Delta t_1 = 200 \mu\text{s}$, the difference densities in the Y_Z area vanish completely, whereas those surrounding Mn4 and Ca increase, and the Mn4–Ca distance further extends to 4.10 Å (Fig. 3a, Extended Data Fig. 3, Extended Data Table 2 and Supplementary Video 3). The results suggest that Mn4(III) of the OEC donates one electron to Y_Z at $\Delta t_1 = 1 \mu\text{s}$ to $\Delta t_1 = 200 \mu\text{s}$. At the completion of Mn4 oxidation by $\Delta t_1 = 200 \mu\text{s}$, a negative difference density emerges on O5, suggesting its instability, which is subsequently stabilized at $\Delta t_1 = 5 \text{ ms}$. In addition, at $\Delta t_1 = 5 \text{ ms}$, a positive difference density appears near Mn1 but outside of the OEC, suggesting the movement of Mn1 away from the OEC. These structural changes might stabilize the positive charge on the OEC.

In correlation with the outward movement of Ca from $\Delta t_1 = 30 \mu\text{s}$ to $\Delta t_1 = 5 \text{ ms}$, one of the carboxyl oxygens of D1-E189 located close to Ca shifts slightly away from Ca. Because the movement of Ca is larger than that of D1-E189, the Ca–D1-E189 distance decreases from 3.02 Å ($\Delta t_1 = 1 \mu\text{s}$) to 2.86 Å ($\Delta t_1 = 5 \text{ ms}$) (Fig. 3a, Extended Data Fig. 3, Extended Data Table 2 and Supplementary Video 3). In addition, W10, which is located in the proximity of D1-E189, becomes disordered in the same time range, and this correlates with the motion of Ca and D1-E189.

Insertion of O6 in the S_2 – S_3 transition

No difference density appears on the OEC at $\Delta t_2 \leq 200 \text{ ns}$, suggesting that no structural changes to the OEC occur in this time range (Fig. 3b and Supplementary Video 4). One notable positive difference density—designated as $O6^*$ —emerges approximately 2.2 Å away from Ca during $\Delta t_2 = 1 \mu\text{s}$ to $\Delta t_2 = 200 \mu\text{s}$, and disappears by $\Delta t_2 = 5 \text{ ms}$, with the concomitant increase of the O6 density from $\Delta t_2 = 200 \mu\text{s}$ to $\Delta t_2 = 5 \text{ ms}$ (Fig. 3b, Extended Data Fig. 4a, Supplementary Table 3 and Supplementary Video 4). These observations suggest that $O6^*$ is the origin of O6, and that $O6^*$ binds to Ca at $\Delta t_2 = 1 \mu\text{s}$ to $\Delta t_2 = 30 \mu\text{s}$, translocates to O6 at $\Delta t_2 = 200 \mu\text{s}$ and completes its translocation by $\Delta t_2 = 5 \text{ ms}$.

At $\Delta t_2 \leq 1 \mu\text{s}$, there are no difference densities among the neighbouring water molecules of $O6^*$, indicating that $O6^*$ does not originate from any stable water molecules nearby. Instead, it is likely to be derived from an aqueous water—specifically, W10—located 2.5 Å away from $O6^*$ in the S_1 state, and becomes disordered at $\Delta t_1 = 30 \mu\text{s}$ – 5 ms (Fig. 3 and Supplementary Video 3). The 2.2-Å distance between $O6^*$ and Ca indicates that $O6^*$ could be a hydroxide ion (OH^-) rather than a water molecule, because water molecules W3 and W4 bind to Ca at distances ranging from 2.4 to 2.6 Å. Indeed, theoretical calculations indicate that an OH^- ion positioned close to $O6^*$ in the S_2 state (Extended Data Fig. 5a,b) exhibits low energy and high stability, whereas the placement of a water molecule is not feasible. The deprotonation of water most likely occurs at $\Delta t_2 = 200 \text{ ns}$ – $1 \mu\text{s}$, during which time the simultaneous existence of Y_Z^{+}/Y_Z and OEC^+ might collectively promote the deprotonation of the $O6^*$ precursor. Consequently, the resulting OH^- ion binds to Ca, neutralizing the positively charged OEC^+ . The achievement of a neutral OEC is crucial for the donation of an electron from the OEC to Y_Z , because it is energetically unfavourable for the OEC^+ to continuously lose one more electron to Y_Z and transform into OEC^{2+} . The subsequent transfer of one electron from the OEC to Y_Z , occurring at $\Delta t_2 = 30 \mu\text{s}$ and $\Delta t_2 = 200 \mu\text{s}$, leads to a decrease in the difference densities at the Y_Z region and a simultaneous increase in the difference densities on the OEC (Fig. 3b, Supplementary Table 3 and Supplementary Video 4). The presence of paired positive and negative difference densities on both sides of Mn1 and Mn4 indicates outward movements of Mn1 and

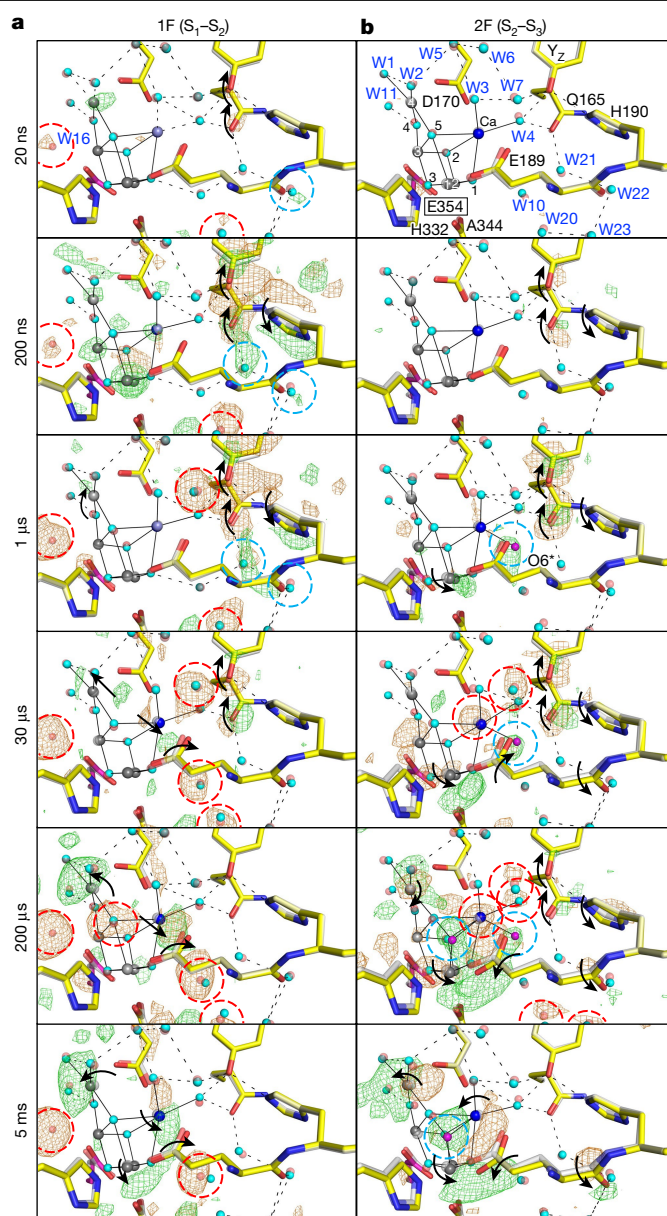


Fig. 3 | Structural dynamics of the OEC during S_1 – S_2 – S_3 transitions. **a, b**, Structures of PSII in the OEC area are superposed with $F_{\text{obs}}(1F) - F_{\text{obs}}(\text{Dark})$ (**a**) and $F_{\text{obs}}(2F) - F_{\text{obs}}(1F)$ (**b**) difference density maps contoured at $+4.0\sigma$ (green) and -4.0σ (orange), with delay times from 20 ns to 5 ms. Residues of CP43 (a subunit of PSII) are shown in magenta and encircled by rectangles. The oxo-oxygen in the OEC and ligand waters are linked to the metal ions by black solid lines. The colour scheme used for other residues and atoms is the same as in Figs. 1 and 2.

Mn4 in the OEC (Fig. 3b and Supplementary Video 4), which results in an increase in the Mn1–Mn4 distance from 4.94 Å ($\Delta t_2 = 30 \mu\text{s}$) to 5.22 Å ($\Delta t_2 = 200 \mu\text{s}$), as well as an increase in the Mn1–Mn3 distance from 3.16 Å ($\Delta t_2 = 30 \mu\text{s}$) to 3.38 Å ($\Delta t_2 = 200 \mu\text{s}$) (Extended Data Fig. 3 and Extended Data Table 2). In addition, the single negative difference density on Ca suggests the disorder of Ca (Fig. 3b and Supplementary Video 4). Of note, at $\Delta t_2 = 200 \mu\text{s}$, while $O6^*$ is still present, a positive difference density emerges in the location of O6, indicating that O6 is incorporated into the OEC. The structural changes to the OEC at $\Delta t_2 = 30 \mu\text{s}$ and $\Delta t_2 = 200 \mu\text{s}$ can be explained as follows: Mn1 undergoes oxidation from Mn1(III) to Mn1(IV), thereby attracting the negatively charged $O6^*$, resulting in its translocation to the O6 position and the disorder of Ca. Simultaneously, Mn1 and Mn4 move outwards to create

room for O6 (the outward movement of Mn1 might also be triggered by its own oxidation). At $\Delta t_2 = 200 \mu\text{s}$, the translocation of O6* is not yet complete, resulting in simultaneous observations of both O6* and O6.

We observed no apparent difference density on W3 at all time points (Fig. 3b, Supplementary Table 3 and Supplementary Video 4), which is inconsistent with a role of W3 as the entry point for the origin of O6 (refs. 7,35,36). W4 also seems an unlikely candidate for an entry point owing to spatial constraints, because W4 needs to pass through W3 to reach the O6 position (Extended Data Fig. 4b). The remaining potential pathway is a direct translocation of O6* to the O6 site (Extended Data Fig. 4b). Although the 3.08-Å distance between D1-E189 and Ca might not allow the passage of O6*, this distance represents the average distance observed both in PSII molecules that have successfully completed the O6* translocation and in those that have not, but not in PSII in which O6* is being translocated. Therefore, this distance might transiently extend when O6* is passing. Furthermore, an OH⁻ ion is smaller than a water molecule, so the direct translocation of O6* (OH⁻) is possible. By $\Delta t_2 = 5 \text{ ms}$, the translocation is completed, and O6 becomes the eighth ligand to Ca and the sixth ligand to Mn1 (Fig. 3b and Supplementary Video 4). The negative difference density near Ca indicates the inward movement of Ca towards the centre of the OEC. By contrast, Mn1 and Mn4 move further outwards from the OEC, which further opens the OEC (Fig. 3b, Extended Data Fig. 3, Extended Data Table 2 and Supplementary Video 4).

Determining the accurate positions of O5 and O6 using electron density alone at the current 2.25-Å resolution is challenging, owing to the influence of mixed populations of different S₂ states and the presence of neighbouring electron-rich metal ions. To refine the structures of OEC at $\Delta t_2 = 200 \mu\text{s}$ and $\Delta t_2 = 5 \text{ ms}$, we chose three O5–O6 distances of 1.9 Å, 2.4 Å and 2.2 Å, respectively, corresponding to oxyl/oxo, hydroxyl/oxo and deprotonated hydroxyl/oxo coupling species³⁷. The optimal positions of O5 and O6 were determined with the smallest residual densities in the $mF_o - DF_c$ map, which showed an O5–O6 distance of 1.9 Å at $\Delta t_2 = 200 \mu\text{s}$, whereas the residual densities at $\Delta t_2 = 5 \text{ ms}$ were almost comparable for the O5–O6 distances of 1.9–2.4 Å (Extended Data Fig. 6). This suggests the existence of a mixed species at room temperature—different from what is observed at low temperature⁶. To maintain consistency, we set the O5–O6 distance at 1.9 Å for both $\Delta t_2 = 200 \mu\text{s}$ and $\Delta t_2 = 5 \text{ ms}$. We note that the OEC at $\Delta t_2 = 5 \text{ ms}$ is more open as compared with the structure predicted by theoretical calculations and the OEC structure solved at cryo-temperature^{6,37}, as evidenced by the lengthened Mn1–Mn3 distance of 3.5 Å observed here. This might leave some room for a hydroxyl/oxo coupling mechanism, and there is a crystallographic debate regarding the existence of O6/Ox in the S₂ structure³⁸ (Supplementary Fig. 1 and Supplementary Discussion).

Water inlet from the O1 channel

We observed previously that 1F leads to the disorder of two water molecules—one in the O1 channel and the other in the O4 channel^{6,25}. The current study reveals the dynamic behaviour of the water molecules in these channels. At $\Delta t_1 = 30 \mu\text{s}$ to 5 ms, disorder of W10 and the concomitant movement of D1-D342 were observed, consistent with the previously solved structure of the S₂ state²⁵ (Extended Data Fig. 7a). At $\Delta t_1 \leq 200 \mu\text{s}$, dynamic difference densities appear in the O1 channel. These span from a five-water cluster located near the OEC to the PsbU-K104–D2-R348 (PsbU is a subunit of PSII) salt bridge near the lumen (Extended Data Fig. 7a). Difference densities appear at $\Delta t_1 = 20 \text{ ns}$ on W20, W22 and the nearby D1-D342 main chain; these are likely to be induced by correlated movements of the neighbouring Y_Z and D1-Q165 (Extended Data Fig. 7a). As Y_Z and D1-Q165 move to a greater extent at $\Delta t_1 = 200 \text{ ns}$ and $\Delta t_1 = 1 \mu\text{s}$, the positive electron density on W22 increases and spreads to cover W21 and W22. Subsequently, Y_Z and D1-Q165 move backwards at $\Delta t_1 = 30 \mu\text{s}$ to $\Delta t_1 = 5 \text{ ms}$, and the difference densities vanish (Extended Data Fig. 7a; see Fig. 3a for a closer view). By

contrast, the difference densities near the main chain of D1-D342 persist from $\Delta t_1 = 20 \text{ ns}$ to $\Delta t_1 = 5 \text{ ms}$, indicating its shift throughout the S₁–S₂ transition. Furthermore, during $\Delta t_1 = 20 \text{ ns}$ to $\Delta t_1 = 200 \mu\text{s}$, movement of the D1-D342 main chain induces disorders or shifts of W20, W24, W52 and D1-E329, which are connected to D1-D342 by hydrogen bonds. At $\Delta t_1 = 30\text{--}200 \mu\text{s}$, a negative difference density arises on W53', which is located in the cavity surrounded by OEC-O1, D1-E189, D1-E329, D1-H332 and D1-D342 (Extended Data Fig. 7a), indicating that W53' becomes further disordered. Here, W53 in the S₁ state is only observable under cryo-temperature conditions (PDB codes: 3WU2 (ref. 2) and 4UB6 (ref. 3)) but is not detectable at room temperature (PDB codes: 5WSS (ref. 4) and 7CJ1 (ref. 25)). Therefore, we denote this invisible water as W53' (Extended Data Fig. 1c and Extended Data Fig. 7a).

A negative difference density appears on the PsbU-K104 carboxy terminal at the O1-channel entrance during $\Delta t_1 = 200 \text{ ns}\text{--}200 \mu\text{s}$ and subsequently disappears by $\Delta t_1 = 5 \text{ ms}$ (Extended Data Fig. 7a). The PsbU-K104–D2-R348 salt bridge might function as a gate for the O1 channel, and the PsbU-K104 disorder implies the breakage or loosening of the salt bridge (Extended Data Fig. 7a), resulting in the opening of the gate and the entry of water into the giant cavity that houses Gol1, W55, W56, W59, W61 and W62 (Extended Data Fig. 7a).

At $\Delta t_2 = 20 \text{ ns}$ to $\Delta t_2 = 200 \text{ ns}$, there is no difference density in the O1 channel (Extended Data Fig. 7b). At $\Delta t_2 = 1 \mu\text{s}$, the most noticeable difference density occurs on O6* (Fig. 4b). When O6* is being prepared and translocated to O6 at $\Delta t_2 = 30 \mu\text{s}$ to $\Delta t_2 = 200 \mu\text{s}$, negative difference densities appear on the main chains of D1-D342, D1-E329, W24, W52, W55 and Gol2, indicating that they are disordered during the O6* translocation. At $\Delta t_2 = 5 \text{ ms}$, the disordered components become ordered again after the completion of the O6* translocation. In addition, paired positive and negative difference densities appeared around CP43-V410 (CP43 is a subunit of PSII), suggesting a rotation of the CP43-V410 side chain by 120° rather than a mere shift as proposed previously⁶ (Extended Data Fig. 7b). In conjunction with the CP43-V410 rotation, a partially occupied water designated as W74 emerges in the proximity of the pre-rotation conformation of CP43-V410 (Extended Data Figs. 5c and 7b). Furthermore, two small positive densities appear near Gol1 and PsbU-K104 at $\Delta t_2 = 5 \text{ ms}$, which suggests that two new water molecules become ordered at the end of the O1 channel after O6 translocation, similar to the findings of a previous study⁶ (Extended Data Fig. 5c).

Structural changes in the O4 channel

W16 is the second water in the O4 channel and is disordered after 1F (Fig. 4a). This disorder is maintained after 2F, until returning to a stable state after 3F (refs. 5–7). Disorder of W16 initiates at $\Delta t_1 = 20 \text{ ns}$, increases progressively, and reaches a maximum at $\Delta t_1 = 200 \mu\text{s}$ (Fig. 4a and Supplementary Table 3). The W16 disorder is expected to be influenced by the charge rearrangement that occurs at $\Delta t_1 = 20\text{--}200 \text{ ns}$, the oxidation of Mn4 at $\Delta t_1 = 1\text{--}30 \mu\text{s}$ and the stabilization of the remaining positive charge on the OEC at $\Delta t_1 = 200 \mu\text{s}\text{--}5 \text{ ms}$ (Fig. 3a). One potential explanation is that the alternation of Mn4 charge influences W11 through O4, leading to the disruption of the hydrogen bond between W11 and W16 and the W16 disorder. The W16 disorder further affects the hydrogen-bonding network at the O4 channel, leading to shifts of W18, W31, W33 and W34 from $\Delta t_1 = 20 \text{ ns}$ to $\Delta t_1 = 5 \text{ ms}$ (Fig. 4a). In addition, when the difference densities in the O4 channel are strongest at $\Delta t_1 = 200 \mu\text{s}$, the main chains of D1-R334–N335–A336 showed slight shifts towards the OEC. Movement of D1-D61 towards the OEC is also observed at $\Delta t_1 = 30 \mu\text{s}\text{--}5 \text{ ms}$ (Fig. 4a).

No noticeable difference densities are observed in the O4 channel at $\Delta t_2 = 20 \text{ ns}\text{--}1 \mu\text{s}$. At $\Delta t_2 = 30 \mu\text{s}$, negative difference densities emerge on W11, CP43-E354 and D1-D61 (Fig. 4b), indicating their instability during this period. The nearby CP43-M356 appears to move toward this region (Fig. 4b), possibly to fill the space. At $\Delta t_2 = 200 \mu\text{s}$, W11 maintains its disorder, whereas CP43-E354, D1-D61 and CP43-M356 are restabilized

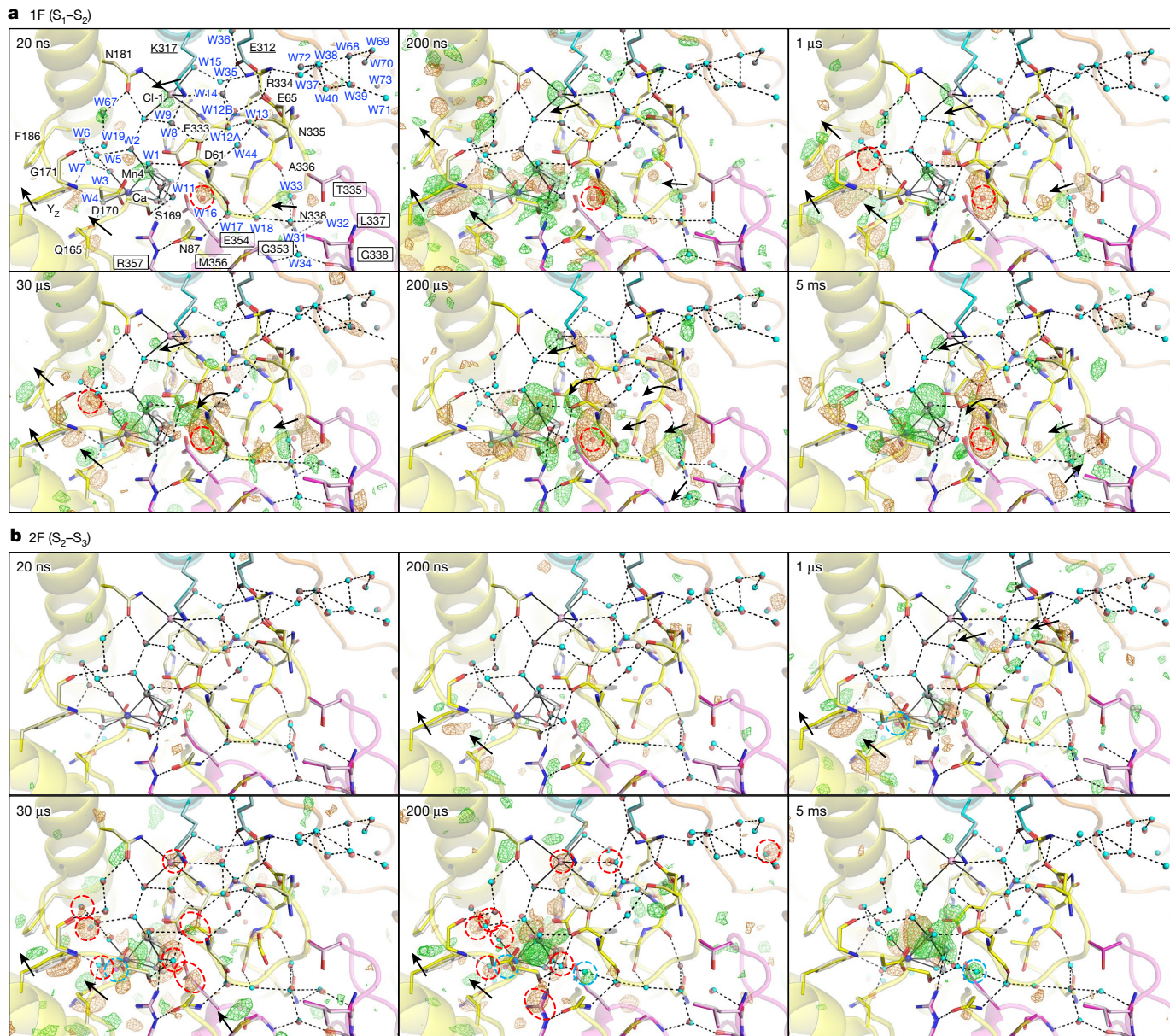


Fig. 4 | Structural dynamics at the O4 and Cl-1 channels during $S_1-S_2-S_3$ transitions. **a, b**, Structures of PSII at the O4 and Cl-1 channels are superposed with $F_{\text{obs}}(1F) - F_{\text{obs}}(\text{Dark})$ (**a**) and $F_{\text{obs}}(2F) - F_{\text{obs}}(1F)$ (**b**) difference density maps contoured at $+3.5\sigma$ (green) and -3.5σ (orange) with delay times from 20 ns to

5 ms. The intermediate structures of D1, D2, CP43 and PsbO proteins are depicted in yellow, cyan, magenta and orange, respectively, and the colours of other atoms are the same as those in Figs. 1 and 2.

(Fig. 4b). CP43-R357, which is located at a hydrogen-bonding distance to O4, becomes disordered at $\Delta t_2 = 200 \mu\text{s}$. All of these residues and water molecules become ordered at $\Delta t_2 = 5 \text{ ms}$ (Fig. 4b). The oxidation of the OEC that takes place at $\Delta t_2 = 30-200 \mu\text{s}$ could potentially contribute to the structural changes on W11, CP43-E354 and CP43-R357; all are directly connected to the OEC.

Roles of Cl-1 in the S-state transitions

Difference densities near Cl-1 are observed at $\Delta t_1 = 20 \text{ ns}-5 \text{ ms}$; however, they fluctuate over time, in contrast to the nearly continuously growing difference densities observed on W16 (Fig. 4a and Supplementary Table 3). The difference densities near Cl-1 arise at $\Delta t_1 = 20 \text{ ns}$, reach a maximum at $\Delta t_1 = 200 \text{ ns}$, decline at $\Delta t_1 = 1-30 \mu\text{s}$, increase again at $\Delta t_1 = 200 \mu\text{s}$ and finally decrease at $\Delta t_1 = 5 \text{ ms}$. Considering the dynamics of the Y_z area and the OEC at $\Delta t_1 = 20 \text{ ns}-5 \text{ ms}$, we hypothesize that

the electrostatic effect of Y_z and the OEC influences Cl-1, causing the fluctuation of the difference densities (Figs. 2a, 3a and 4a and Supplementary Table 3). The difference densities near Cl-1 are observed when Y_z is oxidized to Y_z^{++} at $\Delta t_1 = 20 \text{ ns}$ (Figs. 2a and 4a). These difference densities reach their peaks when Y_z^{++} loses one proton, resulting in the formation of more oxidized Y_z^+ at $\Delta t_1 = 200 \text{ ns}$ (Figs. 2a and 4a). Subsequently, difference densities near Cl-1 decrease during the reduction of Y_z^+ at $\Delta t_1 = 1 \mu\text{s}$ and $\Delta t_1 = 30 \mu\text{s}$. The disruption of the hydrogen-bonding network between Y_z and Cl-1 could also contribute to the decreased signals (Figs. 2a and 4a). As the reduction of Y_z^+ is completed and the OEC is oxidized to OEC $^+$ at $\Delta t_1 = 200 \mu\text{s}$, the difference densities near Cl-1 increase again (Figs. 3a and 4a). The subsequently decreased difference density at $\Delta t_1 = 5 \text{ ms}$ could be attributable to a stabilization effect of the positive charge on the OEC. On the basis of these observations, Cl-1 might actively contribute to stabilizing the positively charged Y_z and OEC during the S_1-S_2 transition.

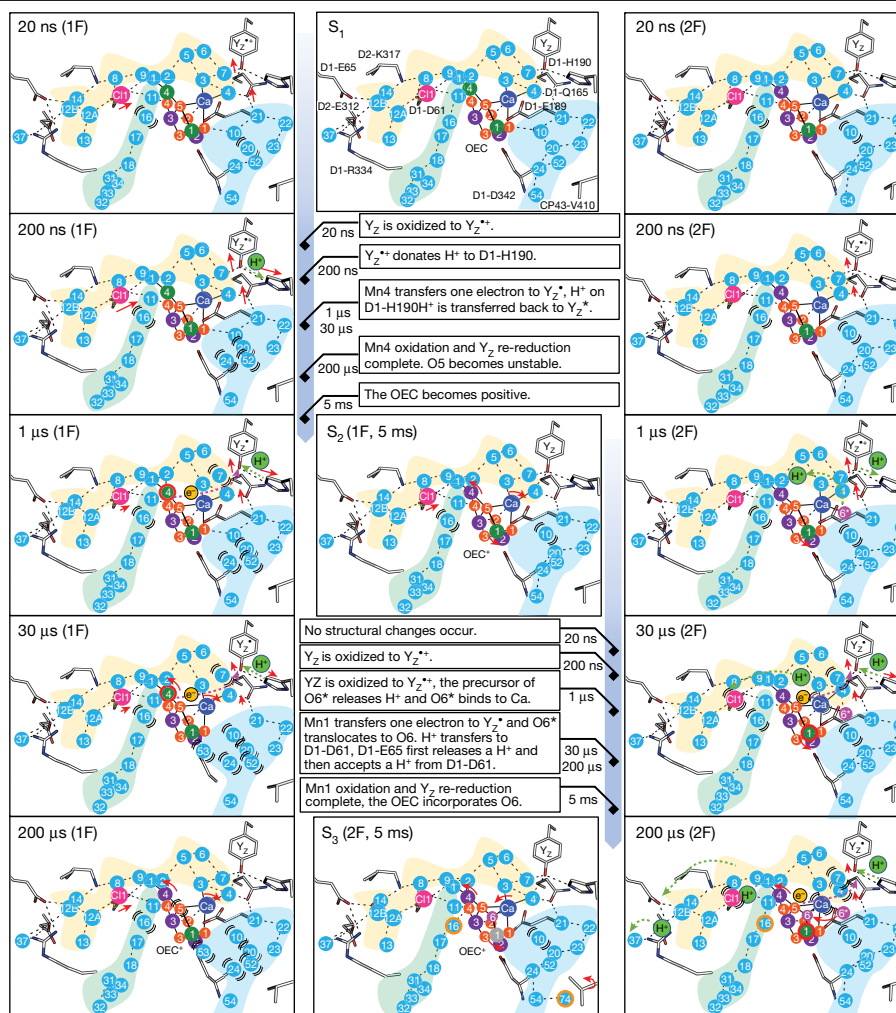


Fig. 5 | Schematic of events occurring during S₁-S₂-S₃ transitions at the electron donor side. The small orange spheres correspond to O1–O5 and are numbered 1 to 5 in the OEC. O6* and O6 are shown as magenta spheres. The larger green, purple and grey spheres represent Mn1–Mn4 with labels 1 to 4. Specifically, the green spheres correspond to Mn(III), the purple spheres correspond to Mn(IV) and the grey sphere represents either Mn(III) or Mn(IV). A red outer ring of the spheres signifies that the Mn ion is undergoing oxidation. The Cl-1, O4 and O1 channels are depicted in yellow, light green and cyan backgrounds, respectively. Water molecules are depicted as cyan spheres,

with their corresponding numbers labelled. Disordered water molecules and other disordered atoms are depicted with arched lines, and an orange outer ring of the water molecules indicate that they become ordered. The red arrows indicate the movements of residues and atoms; the length of the arrows roughly represents the travelled distance for Y₂ and Cl-1. The purple- and green-dotted arrows indicate the movements of electrons and protons, respectively. The proton transfer from Y₂ to D1-H190 takes place between 2F (1 μs) and 2F (30 μs), which was depicted at 2F (1 μs) owing to the absence of time points between 1 μs and 30 μs.

Although paired positive and negative difference densities surrounding the two sides of Cl-1 were observed at $\Delta t_1 = 20 \text{ ns}$ –5 ms (some negative densities are weaker, which cannot be visible at the contour level $\pm 3.5\sigma$), a single negative difference density was observed overlaying Cl-1 at $\Delta t_2 = 30 \mu\text{s}$ and $\Delta t_2 = 200 \mu\text{s}$ (Fig. 4b and Supplementary Table 3). This indicates the disorder of Cl-1 during this time period after 2F (Fig. 4b), which is apparently different from the movements of Cl-1 observed after 1F. These differences show that Cl-1 has different roles in the S₁-S₂ and S₂-S₃ transitions, and the instability of Cl-1 after 2F might reflect the proton transfer along the Cl-1 channel as described below.

Proton transfer through the Cl-1 channel

After 2F, structural changes in the Cl-1 channel are relatively small compared with those at other sites, and take place mainly between $\Delta t_2 = 1 \mu\text{s}$ and $\Delta t_2 = 200 \mu\text{s}$ (Fig. 4b and Extended Data Fig. 8a). At $\Delta t_2 = 1 \mu\text{s}$, W2 and D1-D61 become unstable, as indicated by the negative difference densities on them (Extended Data Fig. 8a), which might be attributable to the release of a proton from the precursor of O6* during this period.

Concomitantly, W44 becomes transiently stable, probably as a result of the movement of D1-E65, which is connected to W44 (Extended Data Fig. 8a). Another structural change occurring at $\Delta t_2 = 1 \mu\text{s}$ is the movement of the D1-H332 to D1-A336 backbones towards the OEC, which probably occurs owing to structural changes in the OEC. At $\Delta t_2 = 30 \mu\text{s}$, a larger number of water molecules in the hydrogen-bonding network become unstable (W1, W3–W7 and W11), and Cl-1 also starts to become unstable (Extended Data Fig. 8a). These structural changes imply that the proton is transferred to D1-D61 (Extended Data Fig. 8b). The movement of the D1-H332 to D1-A336 backbones is transmitted to the D1-R334 and D1-N335 side chains, leading to a shift of D1-R334 towards the OEC. This results in an instability of W14, and could potentially influence the gate between D1-E65, D2-E312 and D1-R334 (refs. 8,17). At $\Delta t_2 = 200 \mu\text{s}$, water molecules in the bulk region (W37, W70 and W73) also become unstable, in addition to the unstable water molecules near the OEC and Cl-1 (W1, W3–W5, W7–W9, W11 and W14) (Extended Data Fig. 8a), suggesting a possible proton transfer to the lumen. The instability of Cl-1 further increases at $\Delta t_2 = 200 \mu\text{s}$, and D1-R334 also exhibits instability (Extended Data Fig. 8a), presumably reflecting the pass of

the proton^{39,40}. By $\Delta t = 5$ ms, the structural changes in the gate area, as well as the high mobilities of water molecules observed at $\Delta t = 200$ μ s, disappear entirely, and Cl-I becomes ordered and returns to its original position (Extended Data Fig. 8). This indicates that the Cl-I channel has been restored and reset to the subsequent S-state transition.

In conclusion, our time-resolved SFX experiments reveal the important roles of protein structural dynamics in electron transfer, water insertion, proton release and O–O bond formation in PSII. We summarize our results in a model presented in Fig. 5, and a detailed discussion is provided in the Supplementary Information.

Online content

Any methods, additional references, Nature Portfolio reporting summaries, source data, extended data, supplementary information, acknowledgements, peer review information; details of author contributions and competing interests; and statements of data and code availability are available at <https://doi.org/10.1038/s41586-023-06987-5>.

- Kok, B., Forbush, B. & McGloin, M. Cooperation of charges in photosynthetic O₂ evolution—I. A linear four step mechanism. *Photochem. Photobiol.* **11**, 457–475 (1970).
- Umena, Y., Kawakami, K., Shen, J.-R. & Kamiya, N. Crystal structure of oxygen-evolving photosystem II at a resolution of 1.9 Å. *Nature* **473**, 55–60 (2011).
- Suga, M. et al. Native structure of photosystem II at 1.95 Å resolution viewed by femtosecond X-ray pulses. *Nature* **517**, 99–103 (2015).
- Suga, M. et al. Light-induced structural changes and the site of O=O bond formation in PSII caught by XFEL. *Nature* **543**, 131–135 (2017).
- Kern, J. et al. Structures of the intermediates of Kok's photosynthetic water oxidation clock. *Nature* **563**, 421–424 (2018).
- Suga, M. et al. An oxyl/oxo mechanism for oxygen-oxygen coupling in PSII revealed by an x-ray free-electron laser. *Science* **366**, 334–338 (2019).
- Ibrahim, M. et al. Untangling the sequence of events during the S₂ → S₃ transition in photosystem II and implications for the water oxidation mechanism. *Proc. Natl Acad. Sci. USA* **117**, 12624–12635 (2020).
- Shen, J.-R. The structure of photosystem II and the mechanism of water oxidation in photosynthesis. *Annu. Rev. Plant Biol.* **66**, 23–48 (2015).
- Romero, E. et al. Two different charge separation pathways in photosystem II. *Biochemistry* **49**, 4300–4307 (2010).
- Cardona, T., Sedoud, A., Cox, N. & Rutherford, A. W. Charge separation in photosystem II: a comparative and evolutionary overview. *Biochim. Biophys. Acta Bioenerg.* **1817**, 26–43 (2012).
- Styring, S., Sjöholm, J. & Mamedov, F. Two tyrosines that changed the world: interfacing the oxidizing power of photochemistry to water splitting in photosystem II. *Biochim. Biophys. Acta Bioenerg.* **1817**, 76–87 (2012).
- Schlodder, E. & Witt, H. T. Stoichiometry of proton release from the catalytic center in photosynthetic water oxidation: reexamination by a glass electrode study at pH 5.5–7.2. *J. Biol. Chem.* **274**, 30387–30392 (1999).
- Suzuki, H., Sugiura, M. & Noguchi, T. Monitoring proton release during photosynthetic water oxidation in photosystem II by means of isotope-edited infrared spectroscopy. *J. Amer. Chem. Soc.* **131**, 7849–7857 (2009).
- Klauss, A., Haumann, M. & Dau, H. Seven steps of alternating electron and proton transfer in photosystem II water oxidation traced by time-resolved photothermal beam deflection at improved sensitivity. *J. Phys. Chem. B* **119**, 2677–2689 (2015).
- Vassiliev, S., Zaraiskaya, T. & Bruce, D. Exploring the energetics of water permeation in photosystem II by multiple steered molecular dynamics simulations. *Biochim. Biophys. Acta Bioenerg.* **1817**, 1671–1678 (2012).
- Sakashita, N., Watanabe, H. C., Ikeda, T., Saito, K. & Ishikita, H. Origins of water molecules in the photosystem II crystal structure. *Biochemistry* **56**, 3049–3057 (2017).
- Hussein, R. et al. Structural dynamics in the water and proton channels of photosystem II during the S₂ to S₃ transition. *Nat. Commun.* **12**, 6531 (2021).
- Shoji, M. et al. Large-scale QM/MM calculations of hydrogen bonding networks for proton transfer and water inlet channels for water oxidation—theoretical system models of the oxygen-evolving complex of Photosystem II. *Adv. Quant. Chem.* **70**, 325–413 (2015).
- Wincencjusz, H., van Gorkom, H. J. & Yocum, C. F. The photosynthetic oxygen evolving complex requires chloride for its redox state S₂ → S₃ and S₃ → S₀ transitions but not for S₀ → S₁ or S₁ → S₂ transitions. *Biochemistry* **36**, 3663–3670 (1997).
- Okamoto, Y., Shimada, Y., Nagao, R. & Noguchi, T. Proton and water transfer pathways in the S₂ → S₃ transition of the water-oxidizing complex in photosystem II: time-resolved infrared analysis of the effects of D1-N298A mutation and NO₃⁻ substitution. *J. Phys. Chem. B* **125**, 6864–6873 (2021).
- Mandal, M., Saito, K. & Ishikita, H. Requirement of chloride for the downhill electron transfer pathway from the water-splitting center in natural photosynthesis. *J. Phys. Chem. B* **126**, 123–131 (2021).
- Bondar, A. N. & Dau, H. Extended protein/water H-bond networks in photosynthetic water oxidation. *Biochim. Biophys. Acta Bioenerg.* **1817**, 1177–1190 (2012).
- Pokhrel, R., Service, R. J., Debus, R. J. & Brudvig, G. W. Mutation of lysine 317 in the D2 subunit of photosystem II alters chloride binding and proton transport. *Biochemistry* **52**, 4758–4773 (2013).
- Suga, M. et al. Time-resolved studies of metalloproteins using X-ray free electron laser radiation at SACLA. *Biochim. Biophys. Acta Gen. Subj.* **1864**, 129466 (2020).
- Li, H. et al. Capturing structural changes of the S₁ to S₂ transition of photosystem II using time-resolved serial femtosecond crystallography. *IUCr* **8**, 431–443 (2021).
- Diner, B. A. & Petrouleas, V. Q400, the non-heme iron of the photosystem II iron-quinone complex. A spectroscopic probe of quinone and inhibitor binding to the reaction center. *Biochim. Biophys. Acta Rev. Bioenerg.* **895**, 107–125 (1987).
- Hienerwadel, R. & Berthomieu, C. Bicarbonate binding to the non-heme iron of photosystem II, investigated by Fourier transform infrared difference spectroscopy and ¹³C-labeled bicarbonate. *Biochemistry* **34**, 16288–16297 (1995).
- Noguchi, T., Suzuki, H., Tsuno, M., Sugiura, M. & Kato, C. Time-resolved infrared detection of the proton and protein dynamics during photosynthetic oxygen evolution. *Biochemistry* **51**, 3205–3214 (2012).
- Berthomieu, C., Hienerwadel, R., Boussac, A., Breton, J. & Diner, B. A. Hydrogen bonding of redox-active tyrosine Z of photosystem II probed by FTIR difference spectroscopy. *Biochemistry* **37**, 10547–10554 (1998).
- Renger, G. Mechanism of light induced water splitting in photosystem II of oxygen evolving photosynthetic organisms. *Biochim. Biophys. Acta* **1817**, 1164–1176 (2012).
- Diner, B. A. & Britt, R. D. in *Photosystem II: The Light-Driven Water-Plastoquinone Oxidoreductase* (eds Wydrzynski, T. J., Satoh, K. & Freeman, J. A.) 207–233 (Springer, 2005).
- Brettel, K., Schlodder, E. & Witt, H. Nanosecond reduction kinetics of photooxidized chlorophyll-a11 (P-680) in single flashes as a probe for the electron pathway, H⁺-release and charge accumulation in the O₂-evolving complex. *Biochim. Biophys. Acta Bioenerg.* **766**, 403–415 (1984).
- Rappaport, F., Blanchard-Desce, M. & Lavergne, J. Kinetics of electron transfer and electrochromic change during the redox transitions of the photosynthetic oxygen-evolving complex. *Biochim. Biophys. Acta Bioenerg.* **1184**, 178–192 (1994).
- Haumann, M. et al. Photosynthetic O₂ formation tracked by time-resolved X-ray experiments. *Science* **310**, 1019–1021 (2005).
- Bovi, D., Narzi, D. & Guidoni, L. The S₂ state of the oxygen-evolving complex of photosystem II explored by QM/MM dynamics: spin surfaces and metastable states suggest a reaction path towards the S₃ state. *Angew. Chem.* **125**, 11960–11965 (2013).
- Askerka, M., Brudvig, G. W. & Batista, V. S. The O₂-evolving complex of photosystem II: recent insights from quantum mechanics/molecular mechanics (QM/MM), extended X-ray absorption fine structure (EXAFS), and femtosecond X-ray crystallography data. *Acc. Chem. Res.* **50**, 41–48 (2017).
- Isobe, H., Shoji, M., Suzuki, T., Shen, J.-R. & Yamaguchi, K. Spin, valence, and structural isomerism in the S₃ state of the oxygen-evolving complex of photosystem II as a manifestation of multimetallic cooperativity. *J. Chem. Theory Comp.* **15**, 2375–2391 (2019).
- Wang, J., Armstrong, W. H. & Batista, V. S. Do crystallographic XFEL data support binding of a water molecule to the oxygen-evolving complex of photosystem II exposed to two flashes of light? *Proc. Natl Acad. Sci. USA* **118**, e32023982118 (2021).
- Debus, R. J. Evidence from FTIR difference spectroscopy that D1-Asp61 influences the water reactions of the oxygen-evolving Mn₄CaO₅ cluster of photosystem II. *Biochemistry* **53**, 2941–2955 (2014).
- Kuroda, H. et al. Proton transfer pathway from the oxygen-evolving complex in photosystem II substantiated by extensive mutagenesis. *Biochim. Biophys. Acta Bioenerg.* **1862**, 148329 (2021).

Publisher's note Springer Nature remains neutral with regard to jurisdictional claims in published maps and institutional affiliations.



Open Access This article is licensed under a Creative Commons Attribution 4.0 International License, which permits use, sharing, adaptation, distribution and reproduction in any medium or format, as long as you give appropriate credit to the original author(s) and the source, provide a link to the Creative Commons licence, and indicate if changes were made. The images or other third party material in this article are included in the article's Creative Commons licence, unless indicated otherwise in a credit line to the material. If material is not included in the article's Creative Commons licence and your intended use is not permitted by statutory regulation or exceeds the permitted use, you will need to obtain permission directly from the copyright holder. To view a copy of this licence, visit <http://creativecommons.org/licenses/by/4.0/>.

© The Author(s) 2024

Methods

Sample preparation

Samples of the PSII microcrystals were prepared as in the previous SFX studies conducted at room temperature^{4,25}, with a few minor adjustments. In brief, cells of the thermophilic cyanobacterium *Thermosynechococcus vulcanus* were grown in a previously described medium^{41–44} in eight 5-l bottles, to a density of $OD_{730\text{ nm}} = 2.5\text{--}3.0$, and collected as described previously^{41–44}. The cells were resuspended in a buffer of 40 mM KH_2PO_4 -KOH (pH 6.8) and 0.4 M mannitol, and treated with 1.21 g l^{-1} lysozyme (FUJIFILM Wako Pure Chemical Corporation) at 37 °C for 90 min with constant shaking. The treated cells were pelleted by centrifugation at 13,700g for 15 min, suspended in 25% (w/v) glycerol, 20 mM HEPES-NaOH (pH 7.0) and 10 mM MgCl_2 (buffer A), and stored at $-80\text{ }^\circ\text{C}$ until use.

The frozen cells were thawed, to which ten folds of a buffer containing 30 mM HEPES-NaOH (pH 7.0) and 10 mM MgCl_2 were added to disrupt the cells by freeze-thawing and osmotic shock. After centrifugation at 13,700g for 15 min, pelleted thylakoids were suspended in 5% (w/v) glycerol, 20 mM HEPES-NaOH (pH 7.0) and 10 mM MgCl_2 . Crude PSII particles were obtained from the thylakoids by a two-step solubilization with a detergent *N,N*-dimethyldodecylamine *N*-oxide (LDAO) (Sigma-Aldrich, 40236-250ML). In the first step, the thylakoids were treated with 0.16% (w/v) LDAO for 5 min on ice, and centrifuged at 43,200g for 60 min. The pellet obtained was suspended in buffer A, and treated with 0.27% (w/v) LDAO for 5 min again. The mixture was centrifuged at 100,000g for 1 h, and the supernatant was recovered. After the addition of 50 (w/v) polyethylene glycol (PEG) 1450 to a final concentration of 15%, crude PSII particles were recovered by centrifugation at 100,000g for 30 min, and resuspended in buffer A^{41–44}.

The PSII crude particles were treated with 1.0% *n*-dodecyl- β -D-maltoside (β -DDM) (FUJIFILM Wako Pure Chemical Corporation, D316) for 5 min, and loaded onto a Q-Sepharose high-performance column (Cytiva) pre-equilibrated with 5% (w/v) glycerol, 30 mM MES-NaOH (pH 6.0), 3 mM CaCl_2 and 0.03% β -DDM (buffer B) in a cooled chamber at 6 °C. The column was washed with eight to ten folds of the column volume of buffer B containing 170 mM NaCl, and eluted with a linear gradient of 12.5 folds of the column volume of 170–300 mM NaCl in buffer B. Elution peaks first appeared for PSII monomer, followed by PSII dimer and PSI monomer, among which PSII dimers were collected. The PSII dimers collected were diluted threefold by buffer B without DDM, and PEG 1450 was added to a final concentration of 13%. The PSII dimers were centrifuged at 100,000g for 30 min, and the pellet was suspended in buffer B without DDM and stored in liquid nitrogen until use^{41–44}.

To make microcrystals of the PSII dimer, the sample was diluted with 20 mM MES-NaOH (pH 6.0), 40 mM MgSO_4 , 20 mM NaCl and 10 mM CaCl_2 , followed by additions of *n*-heptyl- β -D-thioglucopyranoside (HTG) (FUJIFILM Wako Pure Chemical Corporation, H015) and PEG 1450 to final concentrations of 0.85% (w/v) and around 5.50–5.75% (w/v), respectively, at a final concentration of 2.25 mg chlorophyll per ml (refs. 4,6). Microcrystals were grown in a 2.0-ml glass vial (J.G. Finneran Associates, 9800-1232), and 150 μl PSII dimer sample was put into each vial. After standing for 20–30 min at 20 °C, the solution was mixed gently and left to stand for another 10–30 min to allow the microcrystals to grow. In cases in which microcrystals did not appear or appeared in small numbers, the mixing-and-standing step was repeated until enough microcrystals appeared.

After the microcrystals appeared, they were allowed to grow to a maximum size of 100 μm in length for several hours to overnight, following which 150 μl of a crystal storage buffer containing 7% (w/v) PEG 1450, 20 mM MES-NaOH (pH 6.0), 20 mM NaCl, 10 mM CaCl_2 and 0.85% (w/v) HTG was added to stop the growth of the microcrystals. After collection of the microcrystals, the supernatant was discarded, and the microcrystals were stored in the crystal storage buffer at 20 °C

until the X-ray free electron laser (XFEL) experiments. It is important to store the microcrystals in the crystal storage buffer for more than 24 h to ensure high resolution, and they are stable in the crystal storage buffer for at least three days but not more than seven days^{4,6}.

Before conducting the diffraction experiment, a 10 mM potassium ferricyanide solution was added to the PSII microcrystal solution under dim green light, and one pre-flash was given at 20 °C with a laser at a wavelength of 532 nm and an energy of 52 mJ cm^{-2} . The microcrystals were subsequently transferred to 7% (w/v) PEG 1450, 20 mM MES-NaOH (pH 6.0), 20 mM NaCl, 10 mM CaCl_2 , 0.85% (w/v) HTG, 2% dimethyl sulfoxide (DMSO) and 10 mM potassium ferricyanide, and incubated for 10 min at 20 °C. The solution was finally replaced by a cryoprotectant solution containing 10% (w/v) PEG 1450, 10% (w/v) PEG monomethyl ether 5000, 23% (w/v) glycerol, 20 mM NaCl, 10 mM CaCl_2 , 0.85% (w/v) HTG, 2% DMSO and 10 mM potassium ferricyanide for six steps, with each step for 10 min at 20 °C (refs. 4,6).

After replacement of the solution with the cryoprotectant solution, PSII microcrystals were gently mixed with a vacuum grease of a nuclear power grade (Super Lube, 42150)⁴⁵. The ratio of grease to microcrystals was 200 μl to 50 μl (obtained from 4–5 mg chlorophyll), and to avoid physical damage to the microcrystals, the mixing was conducted gently for 2 min. The mixture was exposed to air at 20 °C for around 30–60 min to dehydrate further, before being used for the diffraction experiments at room temperature in darkness⁴. The total time from cryoprotectant replacement to XFEL experiments was one to two hours.

Diffraction experiment

The dark and 1F data, as well as the 1F and 2F time-delayed data, were collected in two independent experiments, resulting in a total of 14 experimental datasets (Extended Data Table 1). Unless otherwise stated, the experimental set-ups were identical for both beamtimes. Diffraction images were obtained using single-shot XFELs collected at the BL2 beamline in the SPring-8 Ångstrom Compact Free Electron Laser (SACLA)⁴⁶. The parameters of the XFEL pulses were as follows: pulse duration 10 fs, energy 10 keV, beam size 3.0 μm (H) \times 3.0 μm (W) and repetition rate 10 Hz (ref. 4). The PSII microcrystals were excited using pump lasers with the following parameters: pulse duration 6 ns (FWHM, Gaussian), energy 42 mJ cm^{-2} , focused spot size 240 μm (top-hat), wavelength 532 nm and frequency rate 10 Hz (ref. 4). To ensure efficient excitation, one laser beam was split into two beams that focused on the same point of the sample from two different directions separated by an angle of 160° (ref. 4).

The injector containing the mixture of PSII microcrystals and grease was carefully inserted into a sample chamber, in which the mixture was ejected from the injector using liquid pressure, ultimately forming a micrometre-sized liquid stream^{47,48}.

The sample flow rate is regulated by adjusting the fluid pressure in the injector. For the 'dark' sample, the flow rate is $1.99\text{ }\mu\text{l min}^{-1}$, whereas for the 'light' samples, it is $7.80\text{ }\mu\text{l min}^{-1}$. As described previously, by maintaining this flow rate, contamination from the prior lasers is effectively avoided²⁵. The dark dataset was obtained by directly exposing the sample stream to XFELs, whereas the 1F and 2F datasets were acquired by illuminating the sample stream with the pump laser first, followed by exposure to the XFELs after a specified delay time Δt . The values of Δt_1 and Δt_2 were set to 20 ns, 200 ns, 1 μs , 30 μs , 200 μs and 5 ms, respectively (Extended Data Fig. 1d). In addition, in the 2F time-delay experiment, the time interval between the first and second flash was set to 5 ms (Extended Data Fig. 1d), which is enough to fully transform the S_1 state to the S_2 state after 1F. The focal centres of the lasers and XFELs were the same for data with a Δt of 20 ns–200 μs , but for data with a Δt of 5 ms, the focal centres of lasers were set 60 μm higher than those of the XFELs to prevent the light-excited microcrystals from escaping the XFEL irradiations after a Δt of 5 ms. Diffraction spots were recorded using a Rayonix MX300-HS detector, which was positioned 240 mm from the sample.

Data processing

During the beamtime, we used Cheetah⁴⁹ (<https://github.com/keit-royam/cheetah>) and CrystFEL (v.0.6.3)^{50,51} to observe and analyse the diffraction images. The analyses provide hit rates, the number of indexed images and approximate resolutions for each dataset, which greatly aided us in devising an effective data-collection strategy. For the processing of diffraction images at the beamline, we at first used approximately 10,000 indexed diffraction images from lysozyme crystals to determine the beam centre and camera length accurately. These parameters were then supplied to CrystFEL for processing the PSII diffraction images. The PSII diffraction images were indexed with 'indexamajig', using the Dirax^{50,51} indexing method with unit-cell parameters of $a = 124.7 \text{ \AA}$, $b = 229.89 \text{ \AA}$, $c = 285.5 \text{ \AA}$, $\alpha = \beta = \gamma = 90^\circ$ adopted from PDB code 5WS5 (ref. 4). The resulting individual intensities were merged using 'process_hkl' and the reflection data were evaluated using 'compare_hkl' (refs. 50,51).

After data collection, 'cctbx.xfel' was used for the indexing and integration of diffraction images, as well as for merging reflections^{52,53}. The accuracy of the beam centre and camera length obtained from CrystFEL were verified by using the program 'cspad.cbf_metrology' (refs. 52,53). The PSII diffraction images were indexed and integrated using 'dials.stills_process' (ref. 54), incorporating the determined detector information and targeted unit-cell parameters mentioned above. Individual reflections were merged by the program 'cxi.merge' (refs. 52,53) with the post-refinement rs2 algorithm, and a filter based on the value of I/σ was not applied so as to include weak signals at high resolutions. The average unit cell, calculated from all of the datasets collected in the same experiment, was used to merge each individual dataset once again. All datasets were processed to a resolution of 2.15–2.30 Å on the basis of the criteria of $CC_{1/2}$ of around 50% (Extended Data Table 1).

Structural refinement for the dark and 1F datasets

Molecular replacement for the dark data was performed using Phaser-MR from PHENIX⁵⁵ with the PSII structure solved at 2.35-Å resolution and at room temperature (PDB code: 5WS5) as the search model, in which water molecules and the OEC were removed⁴. Next, rigid body refinement was applied to the resultant model for one cycle. Subsequently, the B factor was set to 20 for all atoms in the model, and the atomic coordinates and temperature factors of atoms were refined by 'Phenix.refine' in the resolution range of 2.15–20.0 Å, in conjunction with manual modifications by Coot⁵⁶. We iteratively carried out reciprocal space refinement using 'Phenix.refine' and real-space refinement using Coot until the structures of residues and cofactors were confined. Then, the OEC and water molecules were added to the model. Geometric restraints of the OEC are based on the Mn_4CaO_5 cluster solved at 2.15 Å using microcrystals at cryo-temperature (PDB code: 6JLJ)⁶, with a loose distance restraint of $\sigma = 0.06 \text{ \AA}$ on Mn–O and Ca–O distances, whereas no restraints were provided for the Mn–Mn and Mn–Ca distances. Any pre-existing water molecules exhibiting negative $mF_o - DF_c$ signals or lacking $2mF_o - DF_c$ signals were removed from the model. New water molecules were constructed at the positions of positive spherical $mF_o - DF_c$ signals over 4σ , and these water molecules were examined after subsequent rounds of reciprocal and real-space refinements to confirm. Finally, a TLS refinement was applied.

For the refinement of the 1F model in the two-flash time-delay experiments, we assigned a single conformation to the OEC and ligands, considering that the geometry of the OEC does not differ much between S_1 and S_2 states. During the refinement process, the Mn–Mn and Mn–Ca distances were not restrained, whereas the distances of Mn–O and Ca–O were restrained to the values observed in the 1F model solved at 2.15 Å (PDB code: 6JLK)⁶, and refined with a loose restraint ($\sigma = 0.06 \text{ \AA}$). W16 was removed from the model owing to the emergence of a negative $mF_o - DF_c$ signal when W16 was present, even at low occupancy.

Conversely, W10 was retained because its deletion resulted in a significant positive $mF_o - DF_c$ signal at the corresponding location.

Difference-map calculations and structural refinement of intermediates

The phases obtained from the well-refined dark and 1F models were used to calculate isomorphous-difference Fourier maps between dark and 1F time-delayed data, and between 1F and 2F time-delayed data, respectively. Substantial difference densities were detected in the $Q_A - Q_B$, P680, Y_Z and OEC channel regions at each time point, with their locations dynamically varying over time (Figs. 1–4 and Extended Data Fig. 7). To refine the dynamic intermediate structures conveniently and effectively, we devised double conformations for all residues, water molecules and ligands within a spherical range of 20 Å centred on the Ca of the OEC and the non-haem iron, with A and B conformations corresponding to structures of the ground state and intermediate state, respectively. In this case, unstable water molecules and residues in the intermediate state were also built into the structures. Whether to preserve or delete these water molecules is decided by examining the $mF_o - DF_c$ signal. For example, in the case of W16, which became very unstable after 1F, building two conformations resulted in a strong negative signal on W16. Therefore, we deleted the B conformation of W16. On the other hand, for other unstable water molecules, such as W7 and W10, building two conformations did not result in a particularly strong negative $mF_o - DF_c$ signal, so their B conformations were preserved. Populations of S_i state in PSII crystals were estimated to be 0.4/0.6 for S_1/S_2 after 1F and 0.49/0.51 for S_2/S_3 after 2F, on the basis of flash-induced Fourier transform infrared (FTIR) measurements^{4,6,57}. On the basis of these ratios, we constructed the 1F structure by adopting two conformations for those atoms or residues that showed structural changes between S_1 and S_2 . The S_2 -state structure was refined against the density map, whereas the S_1 -state structure was taken from the dark structure solved in the present study. On the other hand, in the 2F data, the structure of PSII that does not advance to the S_3 state is a mixture of S_1 and S_2 . Owing to the small structural changes between S_1 and S_2 , we fixed the structure to the S_2 state for PSII that does not advance to the S_3 state after 2F, and refined the S_3 -state structure against the density map. These assignments do not pose major problems for modelling the structures according to the densities obtained. We refined the xyz coordinates of the B conformation, followed by refining the B factors of both the A and the B conformation, and applied TLS refinement at last.

O6* was modelled as a water molecule with an occupancy of 0.51, without imposing artificial constraints on its distance to Ca and the nearby water molecules. The structures of the OEC containing O6 at $\Delta t_2 = 200 \mu\text{s}$ and $\Delta t_2 = 5 \text{ ms}$ were investigated using three different O5–O6 distances: 1.9 Å, 2.2 Å and 2.4 Å, as indicated by theoretical calculations^{37,58}. The optimal distance was determined by assessing the magnitude of the adjacent $mF_o - DF_c$ signals (Extended Data Fig. 6).

We need to point out that, although the XFEL data collected in the present study have a high quality, and the resolutions obtained are high, uncertainties exist with regard to the subtle structural changes that occur during $S_1 - S_2 - S_3$ transitions, and it is important not to over-interpret the crystallographic data presented in this study.

Estimation of errors in inter-atomic distances

To estimate the errors in the inter-atomic distances, we used the resampling method, creating ten substructures with reduced data multiplicity. Subsequently, we calculated the standard deviations of atom–atom distances within these ten substructures. We resampled our XFEL data by the jackknifing method⁵⁹. We began with a dataset consisting of 100% images and created ten sub-datasets by merging 75% randomly selected images. Subsequently, we refined ten substructures against these sub-datasets. To initiate the refinement of the substructures, we used the well-refined structure derived from the 100% image dataset as our starting model, resetting the temperature factors of all atoms

to 20 Å² and applying simulated annealing. After this, we performed refinements on the rigid body, atom position coordinates, temperature factors and TLS. The standard deviations of atom–atom distances were calculated across the ten substructures, which were used as estimates of the errors associated with the corresponding atom–atom distances in the determined structures (Extended Data Fig. 3).

Density functional theory calculations

An OEC model of the S₃ state for density functional theory (DFT) calculations was constructed from the XFEL model (monomer A) of PSII (PDB code: 6JLL)⁶. This model comprises 408 atoms, including the inorganic Mn₄CaO₅ cluster, 4 terminal aqua/hydroxo ligands at Ca and Mn4, 15 crystal waters along with one extra hydroxide anion referred to as O6*, one chloride anion, and the following amino acid residues: D1-D61, D1-N87, Yz, D1-Q165, D1-S169, D1-D170, D1-N181, D1-V185, D1-F182 (backbone only), D1-E189, D1-H190, D1-N296, D1-N298 (fragment), D2-K317 (fragment), D1-H332, D1-E333, D1-A336, D1-H337, D1-D342, D1-A344 (C terminus), CP43-E354, CP43-R357, CP43-L401, CP43-V410 and CP43-A411. The revision made to the previous computational model^{6,37} involves augmenting it with the incorporation of five water molecules next to O6*, called a 'water wheel', along with four supporting amino acid residues (D1-N296, CP43-L401, CP43-V410 and CP43-A411). Geometric optimizations for the hydroxo form of O6* bound to the Ca site of (Mn^{IV})₃Mn^{III}CaO₅ were carried out at multiplicity 14 (M_s = 13/2) using the B3LYP hybrid functional⁶⁰ augmented with the D3 version of Grimme's empirical dispersion correction and the Becke–Johnson damping function^{61,62}, in combination with the Los Alamos (LANL2DZ) pseudopotential basis set for Ca and Mn and 6-31G(d) for all other atoms^{63–66}. A crucial requirement for the production of meta-stable Ca²⁺-bound hydroxo form of O6*, as displayed in Extended Data Fig. 5a,b, is the absence of a Y_z radical (Tyr_z-O[•]...⁺HN-His190), as the pK_a value of Ca²⁺-bound water (around 12.7 in aqueous solution)^{67,68} might be much higher than that of the histidine residue (6.0) (ref. 69), even within the protein environment.

Reporting summary

Further information on research design is available in the Nature Portfolio Reporting Summary linked to this article.

Data availability

The atomic coordinates and structure factors have been deposited in the PDB under the following accession codes: 8IR5 for OF (dark, ground state) for the Δt1 structures), 8IR6 for Δt1 = 20 ns, 8IR7 for Δt1 = 200 ns, 8IR8 for Δt1 = 1 μs, 8IR9 for Δt1 = 30 μs, 8IRA for Δt1 = 200 μs, 8IRB for Δt1 = 5 ms, 8IRC for 1F (ground state for the Δt2 structures), 8IRD for Δt2 = 20 ns, 8IRE for Δt2 = 200 ns, 8IRF for Δt2 = 1 μs, 8IRG for Δt2 = 30 μs, 8IRH for Δt2 = 200 μs and 8IRI for Δt2 = 5 ms. All other data with a PDB code used in this study are from the PDB data bank.

- Shen, J.-R. & Inoue, Y. Binding and functional properties of two new extrinsic components, cytochrome c-550 and a 12-kDa protein, in cyanobacterial photosystem II. *Biochemistry* **32**, 1825–1832 (1993).
- Shen, J.-R. & Kamiya, N. Crystallization and the crystal properties of the oxygen-evolving photosystem II from *Synechococcus vulcanus*. *Biochemistry* **39**, 14739–14744 (2000).
- Shen, J.-R., Kawakami, K. & Koike H. in *Photosynthesis Research Protocols* (ed. Carpentier, R.) 41–51 (Humana Press, 2011).
- Kawakami, K. & Shen, J.-R. in *Enzymes of Energy Technology* (ed. Armstrong, F.) 1–16 (Academic Press, 2018).
- Sugahara, M. et al. Grease matrix as a versatile carrier of proteins for serial crystallography. *Nat. Methods* **12**, 61–63 (2015).
- Ishikawa, T. et al. A compact X-ray free-electron laser emitting in the sub-ångström region. *Nat. Photonics* **6**, 540–544 (2012).
- Tono, K. et al. Diverse application platform for hard X-ray diffraction in SACLA (DAPHNIS): application to serial protein crystallography using an X-ray free-electron laser. *J. Synchrotron Radiat.* **22**, 532–537 (2015).

- Kubo, M. et al. Nanosecond pump-probe device for time-resolved serial femtosecond crystallography developed at SACLA. *J. Synchrotron Radiat.* **24**, 1086–1091 (2017).
- Nakane, T. et al. Data processing pipeline for serial femtosecond crystallography at SACLA. *J. Appl. Crystallogr.* **49**, 1035–1041 (2016).
- White, T. A. et al. CrystFEL: a software suite for snapshot serial crystallography. *J. Appl. Crystallogr.* **45**, 335–341 (2012).
- White, T. A. et al. Recent developments in CrystFEL. *J. Appl. Crystallogr.* **49**, 680–689 (2016).
- Sauter, N. K., Hattne, J., Grosse-Kunstleve, R. W. & Echols, N. New Python-based methods for data processing. *Acta Crystallogr. D* **69**, 1274–1282 (2013).
- Sauter, N. K. XFEL diffraction: developing processing methods to optimize data quality. *J. Synchrotron Radiat.* **22**, 239–248 (2015).
- Brewster, A. S. et al. Improving signal strength in serial crystallography with DIALS geometry refinement. *Acta Crystallogr. D* **74**, 877–894 (2018).
- Adams, P. D. et al. PHENIX: a comprehensive Python-based system for macromolecular structure solution. *Acta Crystallogr. D* **66**, 213–221 (2010).
- Emsley, P. & Cowtan, K. Coot: model-building tools for molecular graphics. *Acta Crystallogr. D* **60**, 2126–2132 (2004).
- Kato, Y. et al. Fourier transform infrared analysis of the S-state cycle of water oxidation in the microcrystals of photosystem II. *J. Phys. Chem. Lett.* **9**, 2121–2126 (2018).
- Yamaguchi, K. et al. Geometric, electronic and spin structures of the CaMn₄O₅ catalyst for water oxidation in oxygen-evolving photosystem II. Interplay between experiments and theoretical computations. *Coord. Chem. Rev.* **471**, 214742 (2022).
- Nass, K. et al. Structural dynamics in proteins induced by and probed with X-ray free-electron laser pulses. *Nat. Commun.* **11**, 1814 (2020).
- Beeke, A. D. Density-functional thermochemistry. III. the role of exact exchange. *J. Chem. Phys.* **98**, 5648–5646 (1993).
- Grimme, S., Antony, J., Ehrlich, S. & Krieg, H. A consistent and accurate ab initio parametrization of density functional dispersion correction (DFT-D) for the 94 elements H–Pu. *J. Chem. Phys.* **132**, 154104 (2010).
- Grimme, S., Ehrlich, S. & Goerigk, L. Effect of the damping function in dispersion corrected density functional theory. *J. Comput. Chem.* **32**, 1456–1465 (2011).
- Hay, P. J. & Wadt, W. R. Ab initio effective core potentials for molecular calculations. Potentials for the transition metal atoms Sc to Hg. *J. Chem. Phys.* **82**, 270–283 (1985).
- Wadt, W. R. & Hay, P. J. Ab initio effective core potentials for molecular calculations. Potentials for main group elements Na to Bi. *J. Comput. Chem.* **82**, 284–298 (1985).
- Hay, P. J. & Wadt, W. R. Ab initio effective core potentials for molecular calculations. Potentials for K to Au including the outermost core orbitals. *J. Chem. Phys.* **82**, 299–310 (1985).
- Frisch, M. J. et al. Gaussian 09, Revision E. 01 (Gaussian, 2013).
- Hawkes, S. J. All positive ions give acid solutions in water. *J. Chem. Educ.* **73**, 516 (1996).
- Grzybowski, W. Nature and properties of metal cations in aqueous solutions. *Pol. J. Environ. Stud.* **15**, 655–663 (2006).
- Nelson, D. L., Lehninger, A. L. & Cox, M. M. *Lehninger Principles of Biochemistry* 8th edn (W. H. Freeman, 2021).

Acknowledgements We thank T. Nakane and K. Yamashita for their assistance in data processing and structural analysis. The XFEL experiments were performed at SACLA approved by the Japan Synchrotron Radiation Research Institute (JASRI) (proposals 2018A8037, 2018A8010, 2018B8029, 2018B8055, 2019A8019, 2019A8032, 2019B8020, 2019B8028, 2020A8003, 2020A8059, 2021A8003, 2021B8012 and 2022A8007), and we thank the staff at SACLA for their help. The best condition for the collection of diffraction data was determined at beamlines 41XU and 44XU in SPring-8 (proposals 2018B2530, 2019A2559, 2019B2559, 2020A2550, 2021A2550, 2021A2741, 2021B2741, 2021B6618, 2022A2728 and 2022B2728). This research was supported by MEXT KAKENHI JP17H06434 (J.-R.S.) and JP22H04916 (J.-R.S., F.A., K.Y. and M. Suga), JP23H02450, JP22H04754, JP20H03226, JP20H05446 and JST PREST grant JPMJPR18G8 (M. Suga), JP19H05784 (M.K.); a Platform Project for Supporting Drug Discovery and Life Science Research (Basis for Supporting Innovative Drug Discovery and Life Science Research (BINDS)) from AMED under grant number JP21am0101070; and MEXT KAKENHI JP19H05777 (S.I.).

Author contributions J.-R.S. conceived the project. Y.N., F.A., S.K., N.M. and S.Y. made the samples. H.L., Y.N., E.N., K.H., F.L., R.T., F.A., K.K., J.K., Y.S., S.K., H.Y., N.M., H.F., M. Sugahara, M. Suzuki, T.M., T.K., T.N.T., S.Y., L.-J.Y., T.T., M. Suga and J.-R.S. participated in the data collection. K.T., Y.J., T.H., E.N., S.I. and M.Y. developed the data-collection set-up. S.O., D.Y. and M.K. developed the laser set-up. H.L., K.H. and M. Suga processed the diffraction data and analysed the structure. H.I. and K.Y. performed theoretical calculations. H.L., M. Suga and J.-R.S. wrote the manuscript, and all authors contributed to the discussion and improvement of the manuscript.

Competing interests The authors declare no competing interests.

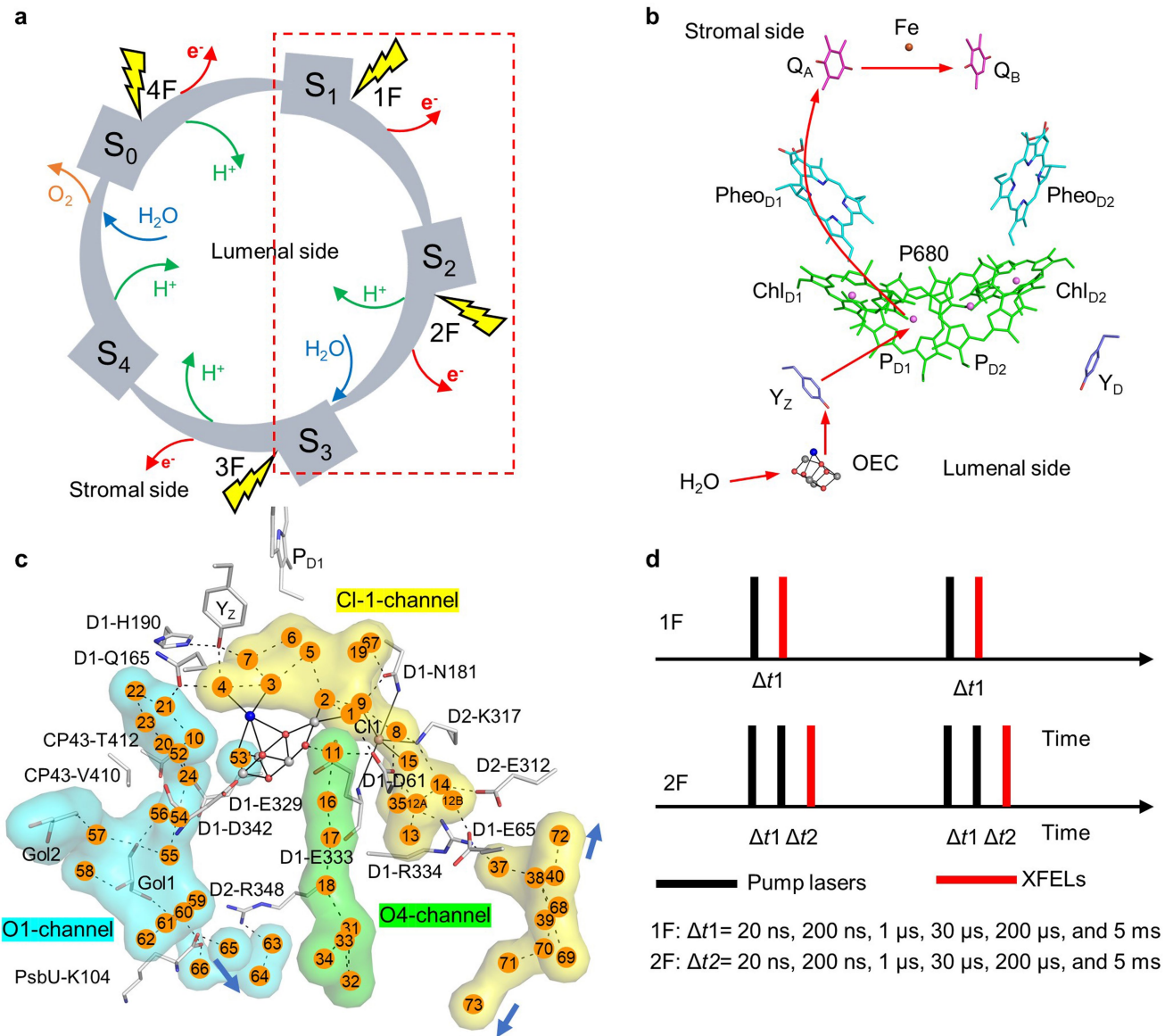
Additional information

Supplementary information The online version contains supplementary material available at <https://doi.org/10.1038/s41586-023-06987-5>.

Correspondence and requests for materials should be addressed to Michihiro Suga or Jian-Ren Shen.

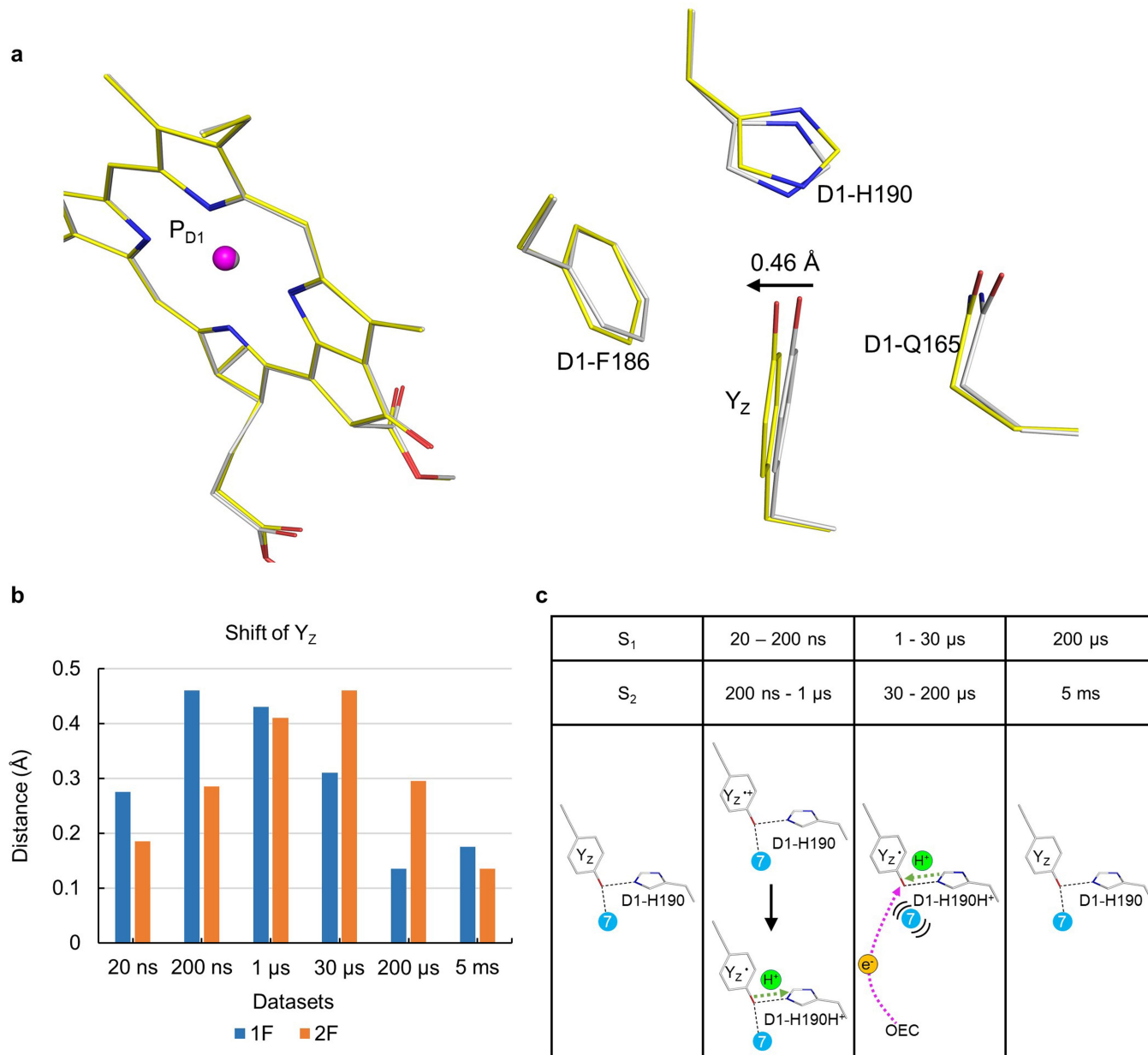
Peer review information Nature thanks Richard Debus, Petra Fromme and the other, anonymous, reviewer(s) for their contribution to the peer review of this work. Peer reviewer reports are available.

Reprints and permissions information is available at <http://www.nature.com/reprints>.



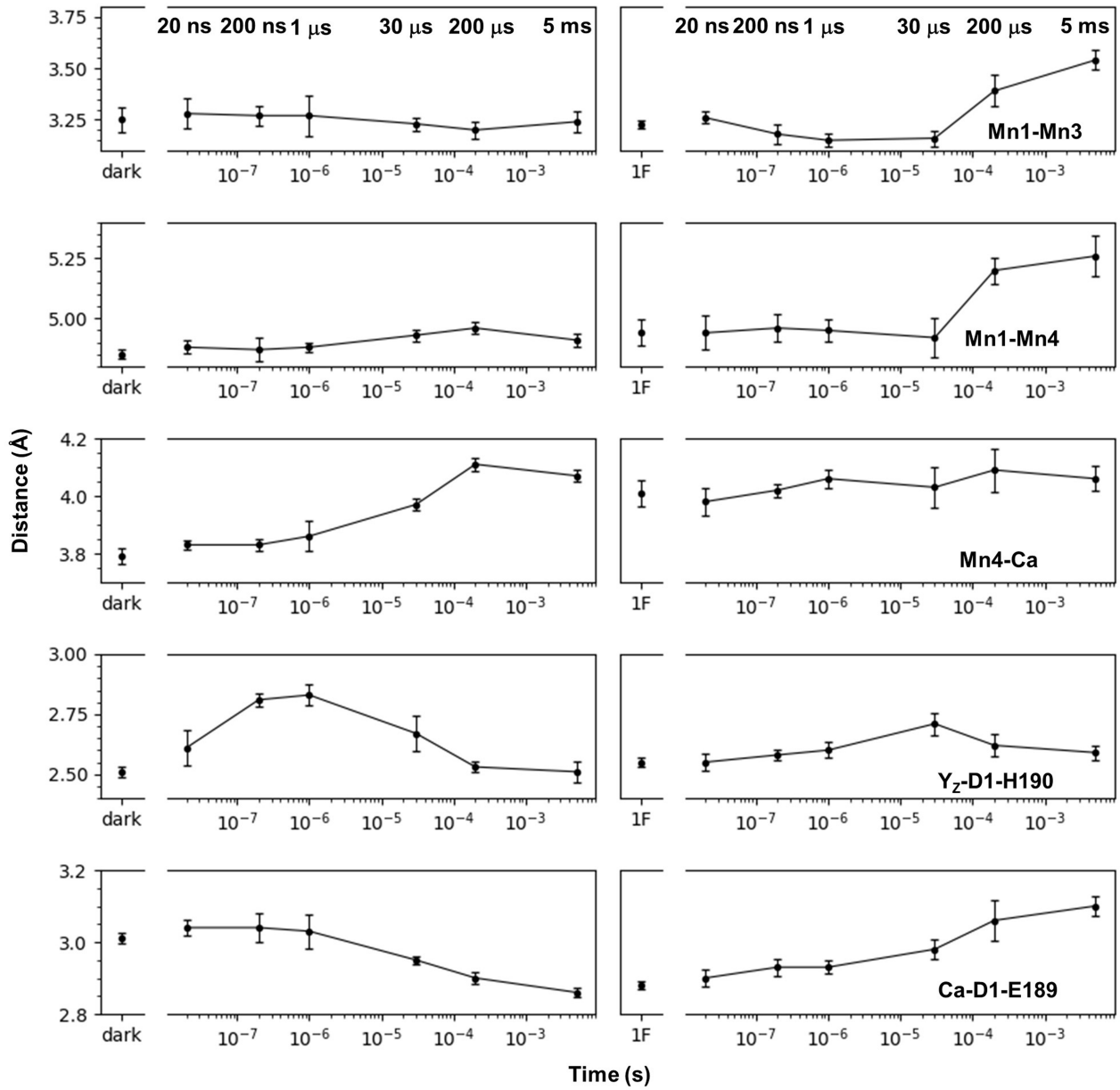
Extended Data Fig. 1 | The Kok cycle and schematic of the present study.
a, The Kok cycle. A rectangular box circled by red, dotted lines highlights the major objective of this study. **b**, Electron transfer pathway in PSII. Red arrows indicate the path of the electron. **c**, Water channels connecting the OEC with the luminal surface. Blue arrows indicate the exits of water channels. 53'

indicates a water molecule not visible in the current model. **d**, Schematic of the pump-probe TR-SFX using one (1F) or two flashes (2F) with delay times ranging from 20 ns to 5 ms. In the 2F experiment, the interval between the first and second flash is 5 ms.



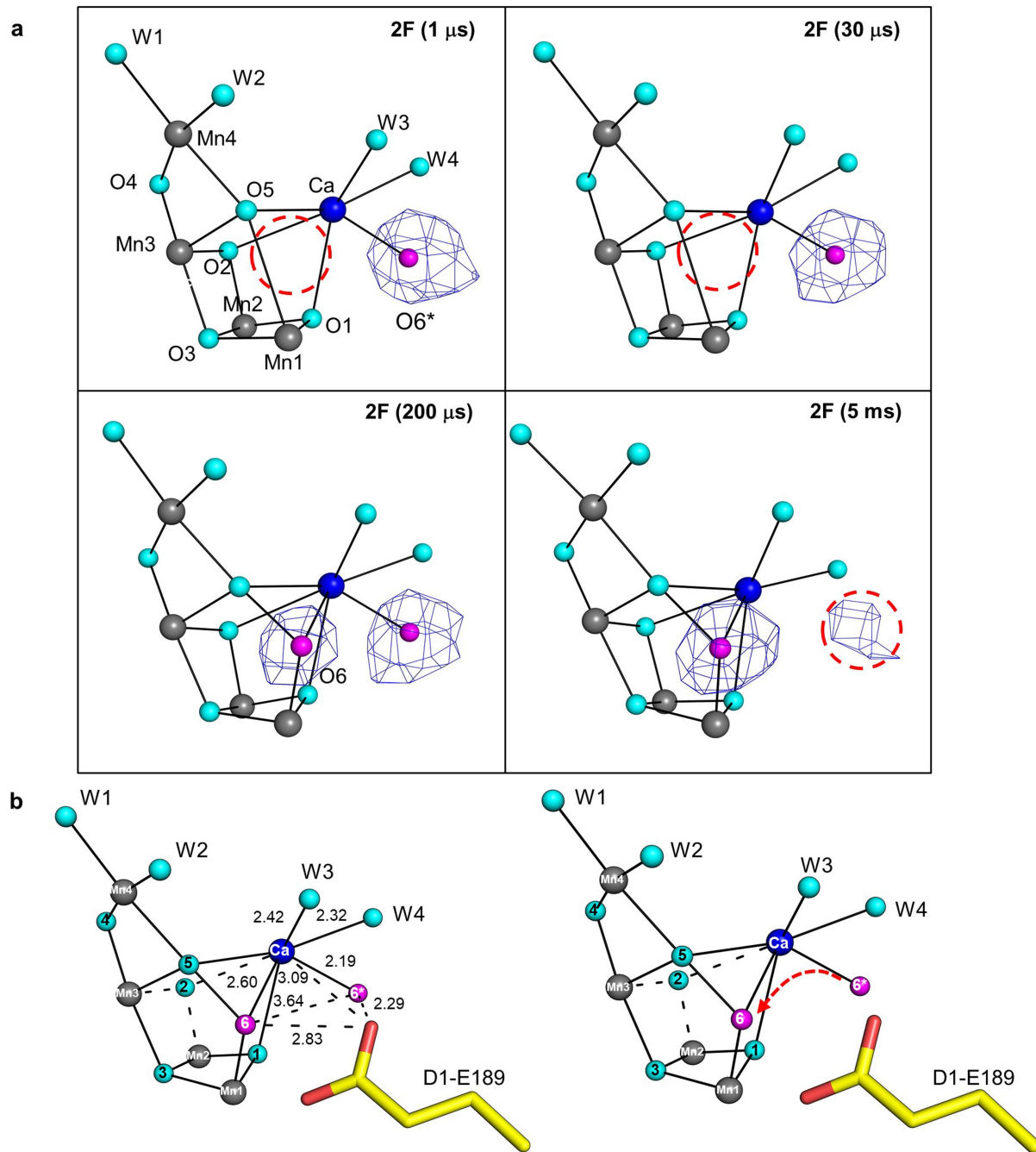
Extended Data Fig. 2 | Redox status of Y_z . **a**, Overlap of the structures of dark (grey stick) and 1F (200 ns) (yellow stick). The black arrow indicates the direction of the Y_z shift, with 0.46 Å representing the shift distance of the phenolic oxygen. **b**, Distances of the shift of the phenolic oxygen at different time points after 1F and 2F. **c**, Redox status of Y_z at various time points following 1F and 2F. The black

arrow at $\Delta t_1 = 20-200$ ns and $\Delta t_2 = 200$ ns-1 μ s (and possibly between 1-30 μ s) indicates the transformation of Y_z . Dotted arrows in green and magenta represent the translocations of proton and electron, respectively. The cyan sphere labelled with '7' represents a water molecule W7, and curves surrounding it at $\Delta t_1 = 1-30$ μ s and $\Delta t_2 = 30-200$ μ s indicate its disordered structure.



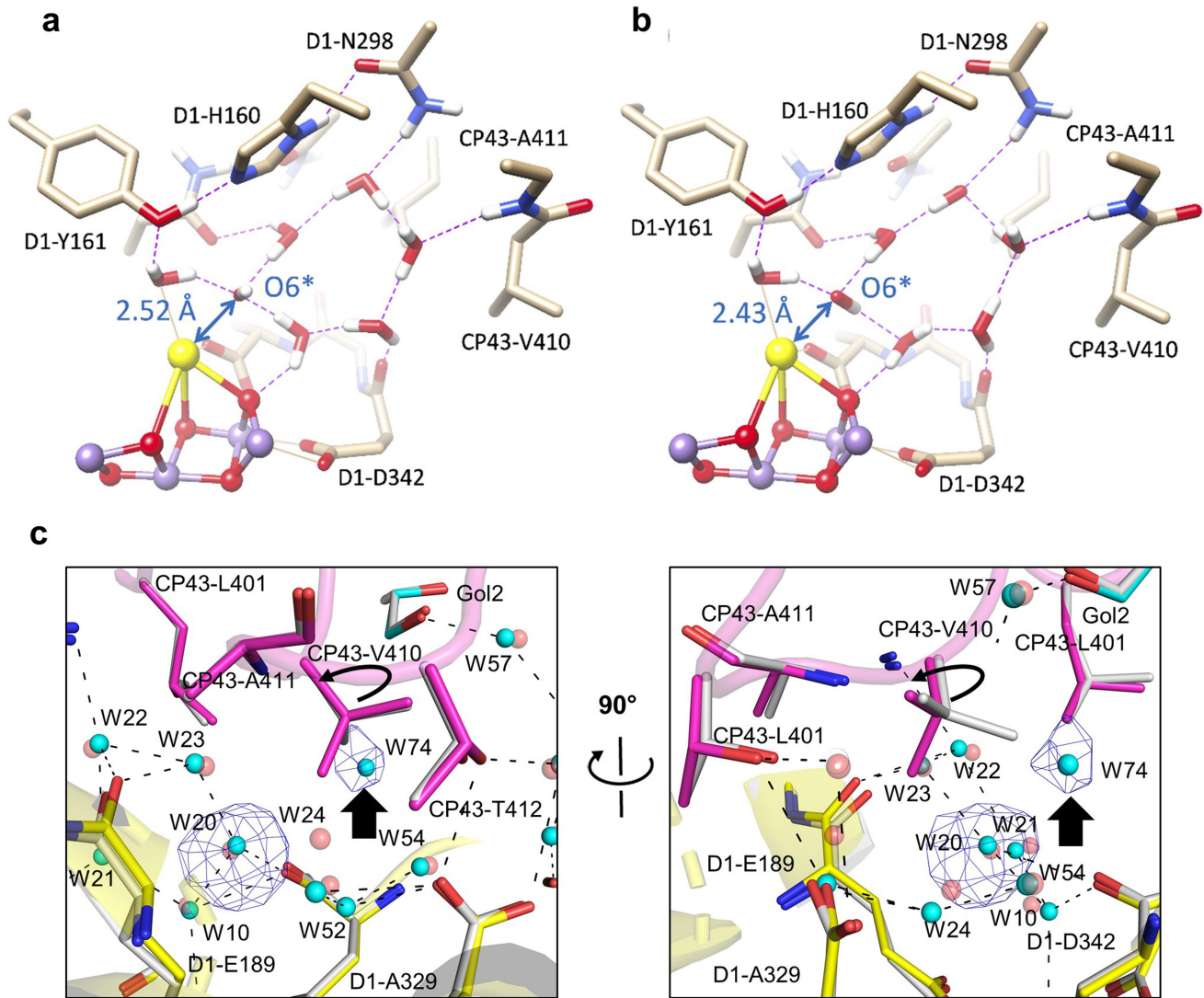
Extended Data Fig. 3 | Variance in inter-atomic distances during S_1 - S_2 - S_3 transitions. Inter-atomic distances are measured at all time points collected after 1F (left) and 2F (right). The mean values for the error bars are obtained with the structures derived from 100% indexed images. The error bars are

estimated using a resampling approach, with the standard deviations determined using ten structures derived from ten sub-datasets, each comprising 75% randomly selected indexed images (see Methods for more details).



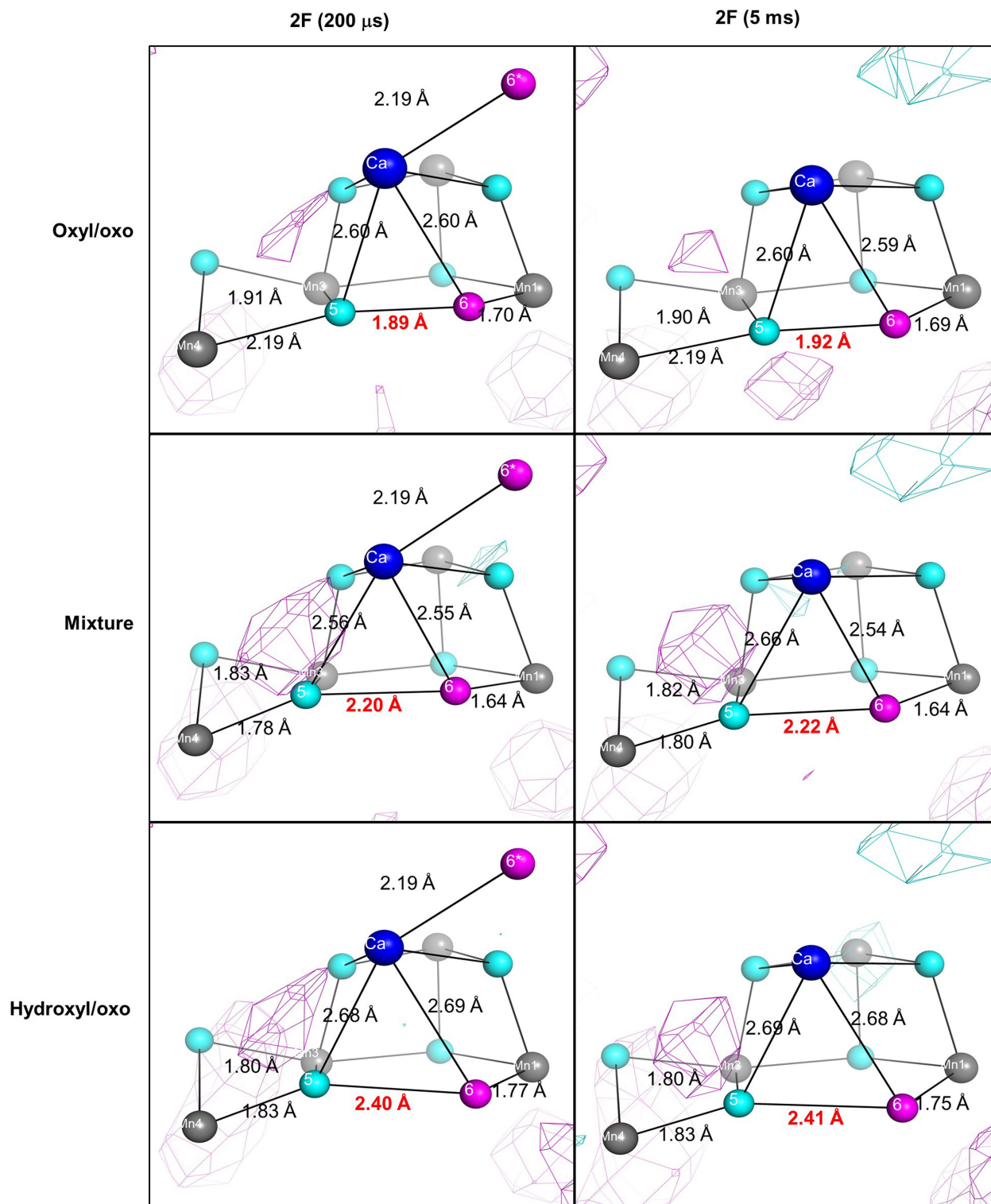
Extended Data Fig. 4 | Translocation of O6* to O6. **a**, Polder omit maps contoured at $+3.0\sigma$ (blue mesh) of O6* and O6 are superposed with OEC models after 2F. The red dashed circles indicate positions where O6 or O6* is either

absent or weak during that specific time point. **b**, Translocation pathway of O6*. Numbers represent the inter-atomic distances in angstrom (\AA). The red line represents the potential translocation pathway for O6*.



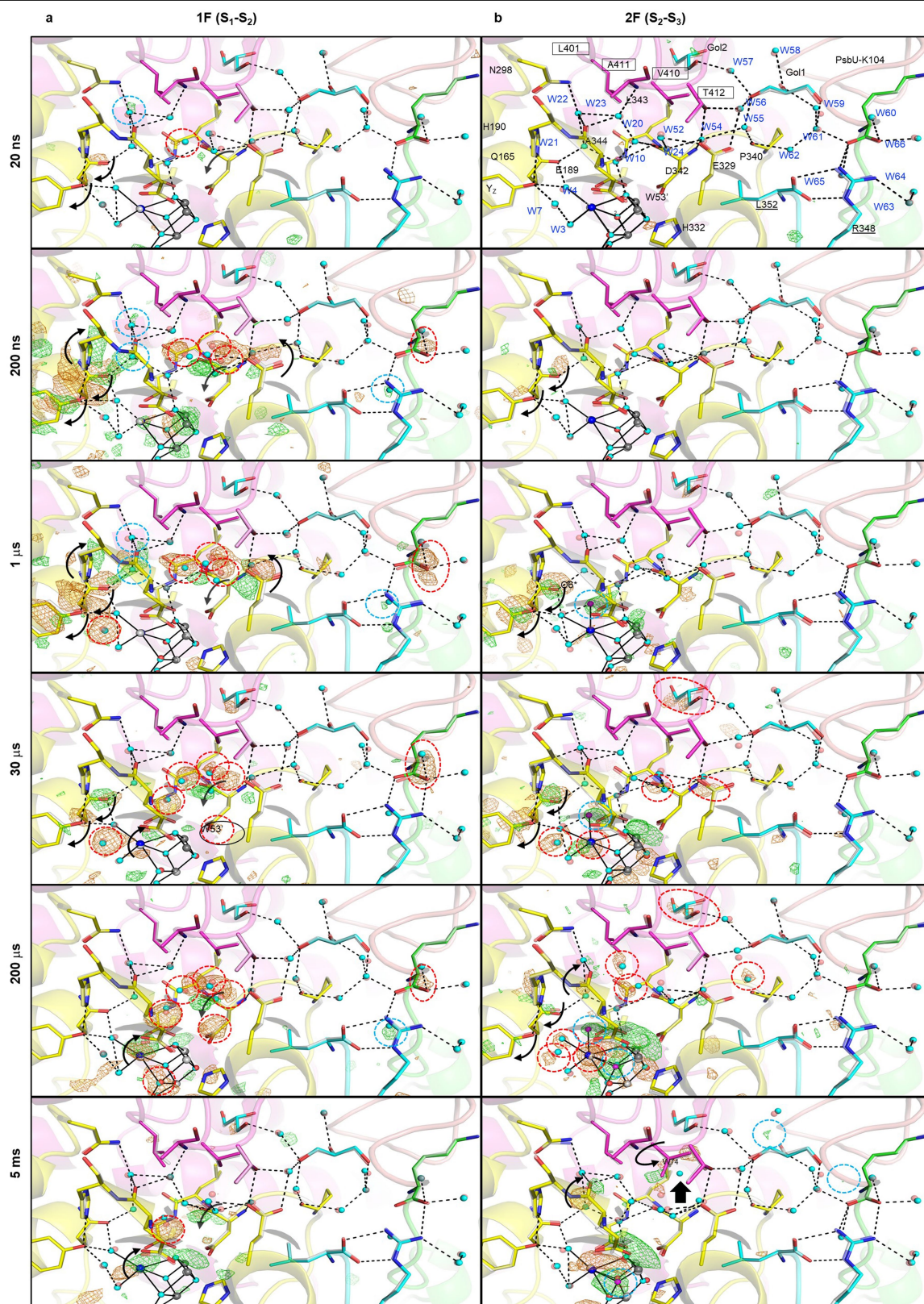
Extended Data Fig. 5 | Two representative hydrogen-bonding arrangements modelled by DFT calculations, and the rotation of CP43-V410 and appearance of one new water molecule. a, b, O6* is modelled as a hydroxide anion bound to Ca²⁺ in the S₂ state: one having a hydrogen bond between O6* and Glu189 (not depicted) (a), and the other one lacking this hydrogen bond (b). It is unstable if

O6* is assumed to be a water molecule. Hydrogen atoms bonded to carbon atoms are omitted for clarity. c, Polder omit maps on W20 and W74 contoured at +3.5σ (blue mesh) superimposed with PSII structures of 1F state (grey sticks and red spheres) and 2F (5 ms) (magenta sticks for CP43 and yellow sticks for D1, as well as cyan spheres for water molecules).



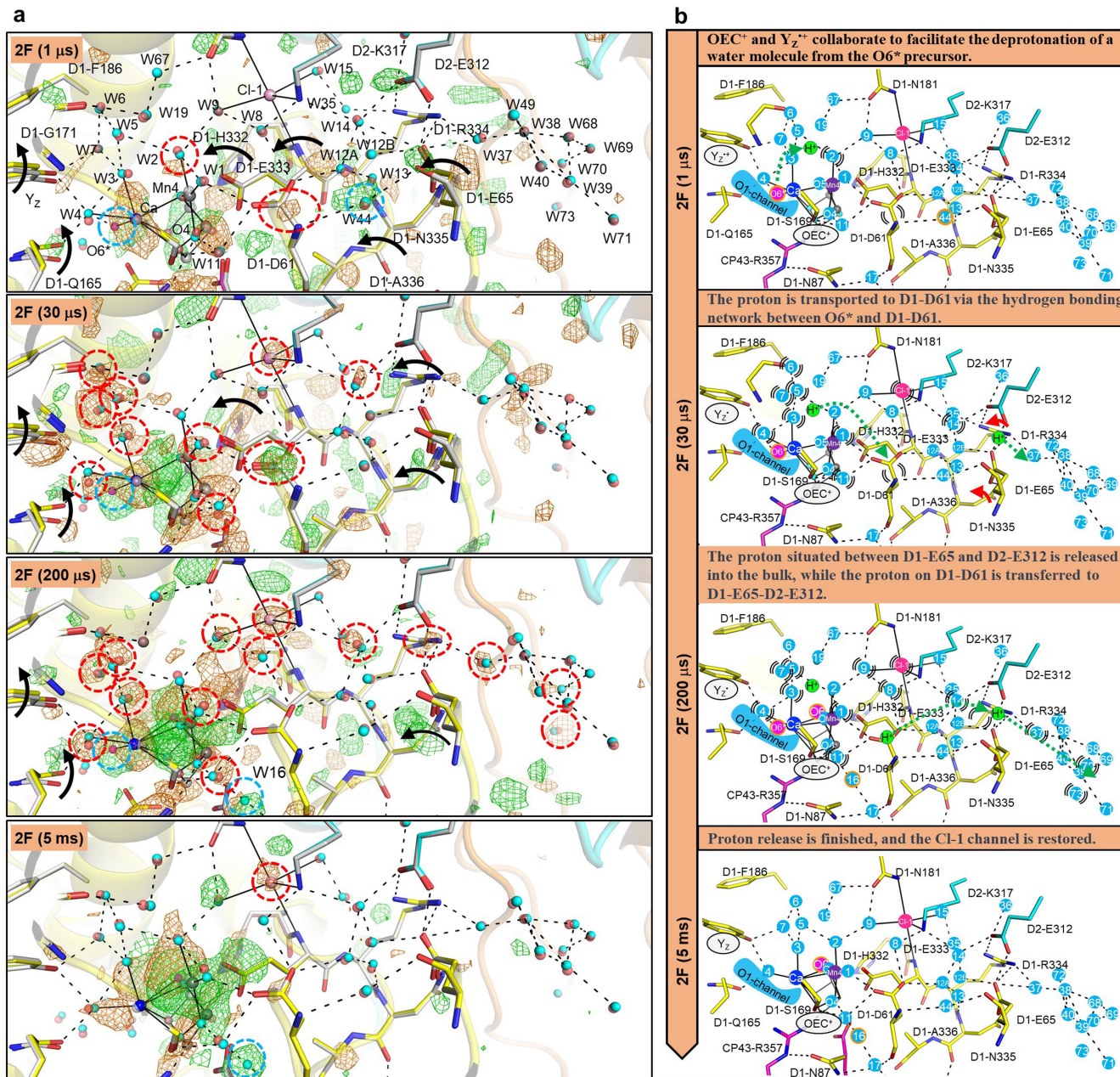
Extended Data Fig. 6 | Examinations of the oxyl/oxo and hydroxyl/oxo species between O5 and O6. The $mF_o - DF_c$ maps contoured at $+2.5\sigma$ (cyan) and -2.5σ (magenta) superposed with OEC structures of 2F (200 μ s) (left) and 2F (5 ms) (right). O5/O6 at distances of 1.9 Å (oxyl/oxo, upper side), 2.4 Å (hydroxyl/

oxo, bottom) and 2.2 Å (mixture of the two coupling species, middle) are examined. On the basis of the residual densities, the distance of 1.9 Å fits best with the electron density at 200 μ s, whereas it is difficult to distinguish between the distances of 1.9 Å–2.4 Å at 5 ms.



Extended Data Fig. 7 | Structural dynamics at the O1 channel during S_1 - S_2 - S_3 transitions. **a, b**, Structures of PSII at the O1 channel are superposed with $F_{\text{obs}}(1F) - F_{\text{obs}}$ (dark) (**a**) and $F_{\text{obs}}(2F) - F_{\text{obs}}(1F)$ (**b**) difference density maps contoured at $+4.0\sigma$ (green) and -4.0σ (orange), with delay times from 20 ns to 5 ms. The intermediate structures of D1, D2, CP43, PsbU and PsbV proteins are depicted in yellow, cyan, magenta, green and pink, respectively. Water molecule

W53 in the S_1 state is only observable under cryo-temperature conditions (PDB codes: 3WU2 and 4UB6) and is not detectable at room temperature (PDB codes: 5WS5 and 7CJI). Because the protein environment around W53 is the same regardless of temperature, W53 is considered present but fluctuating. Therefore, in this study, we denote this invisible water as W53'.



Extended Data Fig. 8 | Structural changes at the Cl-1 channel and proton release pathways after 2F. a, Structures of PSII at Cl-1 channels superposed with $F_{\text{obs}}(2F) - F_{\text{obs}}(1F)$ difference densities contoured at $+3.0\sigma$ (green) and -3.0σ (orange), with delay times from 1 μs to 5 ms. The 1F model is depicted in grey, and intermediate structures of D1, D2, CP43 and PsbO proteins are depicted in yellow, cyan, magenta and orange, respectively. Water molecules at their ground states and intermediate states are depicted in red and cyan spheres, respectively. O6* and O6 are represented by magenta spheres. Black dotted lines represent hydrogen bonds. Black solid lines link the oxo-oxygen in the OEC and the ligand water to the metal ions, as well as ligand residues and water

molecules to Cl-1. Black arrows indicate structural changes. Disordered water and residues are encircled by red dotted lines, and ordered water molecules in the intermediate structures are encircled by cyan dotted lines. **b,** Possible proton release pathways after 2F. Water molecules are depicted as cyan spheres, with their corresponding numbers labelled. Disordered water molecules, Cl-1 and residues are depicted with arched lines, and an orange outer ring around water molecules indicates that they became ordered. The red arrows indicate the movements of residues. The green dotted arrows indicate the movements of protons.

Extended Data Table 1 | Data processing and structure refinement statistics

Data set	Dark	1F (20 ns)	1F (200 ns)	1F (1 μs)	1F (30 μs)	1F (200 μs)	1F (5 ms)	1F	2F (20 ns)	2F (200 ns)	2F (1 μs)	2F (30 μs)	2F (200 μs)	2F (5 ms)	
Wavelength (Å)				1.24							1.24				
No. of collected images	250,748	127,254	145,599	187,489	118,559	186,590	77,543	244,369	197,256	225,474	185,967	104,358	110,258	89,971	
No. of hit images	105,314	62,354	65,520	61,871	54,537	65,307	32,568	69,520	66,006	70,063	72,171	41,691	30,754	44,134	
No. of indexed images	61,207	43,511	48,580	42,595	41,261	46,061	24,670	55,155	50,078	56,728	59,038	33,962	23,851	34,176	
Space group				P2 ₁ 2 ₁ 2 ₁							P2 ₁ 2 ₁ 2 ₁				
Cell dimension (Å)			a = 125.75, b = 231.60, c = 288.28								a = 125.77, b = 231.76, c = 288.58				
Resolution (Å)	47.45-2.15 (2.19-2.15) [†]	47.45-2.20 (2.24-2.20)	47.45-2.25 (2.29-2.25)	47.45-2.25 (2.29-2.25)	47.45-2.20 (2.24-2.20)	47.45-2.20 (2.24-2.20)	47.45-2.30 (2.34-2.30)	47.45-2.25 (2.29-2.25)	47.45-2.30 (2.34-2.30)	47.45-2.25 (2.29-2.25)	47.45-2.25 (2.29-2.25)	47.45-2.30 (2.34-2.30)	47.45-2.25 (2.29-2.25)	47.45-2.25 (2.29-2.25)	
Unique reflections	453,468 (22,435)	427,344 (21,214)	399,706 (19,836)	399,706 (19,836)	427,344 (21,214)	427,344 (21,214)	374,348 (18,515)	399,706 (19,836)	374,348 (18,515)	399,706 (19,836)	399,706 (19,836)	374,348 (18,515)	399,706 (19,836)	399,706 (19,836)	
Multiplicity	597.1 (231.1)	404.4 (197.3)	477.5 (280.0)	381.7 (222.7)	402.1 (195.0)	401.2 (192.5)	237.9 (153.7)	450.8 (229.4)	306.5 (189.4)	514.4 (265.7)	525.7 (270.9)	301.3 (186.7)	210.1 (107.8)	304.3 (154.8)	
Completeness (%)	100.0 (100.0)	100.0 (100.0)	100.0 (100.0)	100.0 (100.0)	100.0 (100.0)	100.0 (100.0)	100.0 (100.0)	100.0 (100.0)	100.0 (100.0)	100.0 (100.0)	100.0 (100.0)	100.0 (100.0)	100.0 (100.0)	100.0 (100.0)	
Mean I/σ (I)	75.2 (1.3)	56.0 (1.1)	59.9 (1.5)	52.7 (1.3)	58.6 (1.4)	53.5 (1.2)	48.5 (1.6)	61.2 (1.5)	49.7 (1.5)	64.8 (1.6)	63.6 (1.4)	56.5 (1.7)	50.6 (1.4)	52.9 (1.5)	
Wilson B-factor (Å ²)	62.3	48.7	48.8	49.2	63.6	48.4	65.6	62.4	64.9	62.9	63.9	64.3	63.7	63.0	
R-split (%) [‡]	5.2 (67.5)	6.8 (75.9)	6.4 (65.8)	7.2 (69.6)	7.3 (68.1)	7.0 (74.9)	9.1 (64.6)	8.2 (67.1)	9.4 (69.2)	7.6 (66.6)	7.1 (69.1)	10.4 (67.7)	10.8 (74.5)	9.5 (72.5)	
CC1/2 (%)	99.7 (59.2)	99.5 (47.9)	99.6 (49.2)	99.4 (53.0)	99.4 (58.6)	99.5 (49.2)	99.1 (59.9)	99.3 (52.6)	99.1 (54.3)	99.4 (56.0)	99.5 (55.4)	98.7 (53.9)	98.6 (47.8)	99.0 (51.6)	
Structure refinement															
Resolution range (Å)	19.98-2.15 (2.23-2.15)	19.98-2.20 (2.28-2.20)	19.98-2.25 (2.33-2.25)	19.98-2.25 (2.33-2.25)	19.98-2.20 (2.28-2.20)	19.98-2.20 (2.28-2.20)	19.98-2.30 (2.38-2.30)	19.99-2.25 (2.33-2.25)	19.99-2.30 (2.38-2.30)	19.99-2.25 (2.33-2.25)	19.99-2.25 (2.33-2.25)	19.99-2.30 (2.38-2.30)	19.99-2.25 (2.33-2.25)	19.99-2.25 (2.33-2.25)	
R-work	0.145 (0.334)	0.143 (0.336)	0.146 (0.320)	0.146 (0.321)	0.140 (0.312)	0.142 (0.334)	0.139 (0.291)	0.145 (0.303)	0.142 (0.305)	0.139 (0.298)	0.140 (0.313)	0.142 (0.294)	0.143 (0.303)	0.142 (0.303)	
R-free	0.175 (0.361)	0.179 (0.370)	0.186 (0.345)	0.180 (0.349)	0.176 (0.349)	0.178 (0.367)	0.180 (0.326)	0.180 (0.334)	0.184 (0.340)	0.177 (0.328)	0.177 (0.342)	0.181 (0.329)	0.183 (0.339)	0.182 (0.338)	
Number of non-H atoms	52978	62674	62674	62674	62674	62674	62674	52977	62600	62600	62602	62602	62605	62604	
Macromolecules	41835	49244	49244	49244	49244	49244	49244	41835	49173	49173	49173	49173	49173	49173	
Ligands	9317	11275	11275	11275	11275	11275	11275	9317	11275	11275	11275	11275	11277	11277	
Solvent	1826	2155	2155	2155	2155	2155	2155	1825	2152	2152	2154	2154	2155	2154	
Protein residues	5289	5289	5289	5289	5289	5289	5289	5289	5289	5289	5289	5289	5289	5289	
RMS (bonds) (Å)	0.008	0.009	0.009	0.009	0.009	0.009	0.009	0.008	0.009	0.009	0.009	0.009	0.009	0.009	
RMS (angles) (degree)	1.26	1.28	1.28	1.28	1.28	1.28	1.29	1.27	1.30	1.30	1.32	1.31	1.29	1.29	
Ramachandran favored (%)	97.83	97.79	97.81	97.81	97.91	97.83	97.81	97.83	97.64	97.89	97.66	97.69	97.87	97.81	
Ramachandran allowed (%)	1.98	2.04	2.02	2.02	1.92	2.00	2.00	2.00	2.17	1.94	2.19	2.15	1.96	2.02	
Ramachandran outliers (%)	0.19	0.17	0.17	0.17	0.17	0.17	0.19	0.17	0.19	0.17	0.15	0.15	0.17	0.17	
Rotamer outliers (%)	2.16	2.15	2.15	2.15	2.21	2.27	2.15	2.41	2.29	2.29	2.14	2.19	2.21	2.16	
Clashscore	4.70	5.00	5.13	5.13	4.99	5.02	5.39	4.54	5.20	4.96	5.02	5.19	4.88	4.75	
Average B-factor (Å ²)	65.71	65.06	65.31	65.56	65.26	65.08	65.54	63.81	63.61	64.11	64.46	65.35	63.89	63.19	
Macromolecules	63.94	62.96	63.24	63.46	63.13	62.94	63.47	62.63	61.88	62.35	62.62	63.59	62.10	61.43	
Ligands	73.23	73.82	73.99	74.33	74.15	74.07	74.32	69.16	70.97	71.63	72.35	72.89	71.55	70.69	
Solvent	67.77	67.08	67.09	67.56	67.45	66.95	67.00	63.66	64.54	65.13	65.26	66.10	64.75	63.91	
PDB code	8IR5	8IR6	8IR7	8IR8	8IR9	8IRA	8IRB	8IRC	8IRD	8IRE	8IRF	8IRG	8IRH	8IRI	

[†]Values in parentheses indicate those for the highest-resolution shells. [‡]R_{split} = $\sqrt{2} \Sigma |I_{\text{even}} - I_{\text{odd}}| / \Sigma (I_{\text{even}} + I_{\text{odd}})$.

Extended Data Table 2 | Atomic distances at various time points after 1F or 2F

Atom-Atom distances	Mono-mer	Dark	1F (20 ns)	1F (200 ns)	1F (1 μ s)	1F (30 μ s)	1F (200 μ s)	1F (5 ms)	1F	2F (20 ns)	2F (200 ns)	2F (1 μ s)	2F (30 μ s)	2F (200 μ s)	2F (5 ms)
Fe-BCT_O1	A	2.18	2.18	2.17	2.22	2.21	2.28	2.36	2.33	2.46	2.40	2.39	2.21	2.32	2.28
	B	2.13	2.10	2.17	2.22	2.28	2.41	2.49	2.28	2.37	2.34	2.20	2.19	2.39	2.27
	Ave.	2.16	2.14	2.17	2.22	2.25	2.35	2.43	2.31	2.42	2.37	2.30	2.20	2.36	2.28
Fe-BCT_O2	A	2.13	2.24	2.40	2.28	2.42	2.35	2.29	2.34	2.17	2.32	2.42	2.44	2.22	2.28
	B	2.42	2.52	2.61	2.53	2.61	2.50	2.59	2.49	2.60	2.52	2.61	2.59	2.38	2.53
	Ave.	2.28	2.38	2.51	2.41	2.52	2.43	2.44	2.42	2.39	2.42	2.52	2.52	2.30	2.41
D1-Y246-BCT_O1	A	3.15	3.17	3.04	3.01	2.98	3.02	2.69	2.90	2.91	3.02	3.15	3.23	3.14	2.98
	B	3.26	3.42	3.27	3.23	3.17	3.15	2.94	3.17	3.10	3.24	3.40	3.32	3.04	3.18
	Ave.	3.21	3.30	3.16	3.12	3.08	3.09	2.82	3.04	3.01	3.13	3.28	3.28	3.09	3.08
Mn1-Mn3	A	3.19	3.21	3.24	3.20	3.20	3.17	3.22	3.22	3.27	3.17	3.16	3.18	3.36	3.53
	B	3.29	3.34	3.28	3.34	3.26	3.22	3.27	3.23	3.26	3.20	3.15	3.14	3.39	3.52
	Ave.	3.24	3.28	3.26	3.27	3.23	3.20	3.25	3.23	3.27	3.19	3.16	3.16	3.38	3.53
Mn1-Mn4	A	4.84	4.84	4.90	4.89	4.92	4.93	4.92	4.97	5.02	5.02	5.00	5.03	5.22	5.33
	B	4.83	4.91	4.83	4.86	4.93	4.97	4.91	4.88	4.87	4.91	4.92	4.85	5.22	5.23
	Ave.	4.84	4.88	4.87	4.88	4.93	4.95	4.92	4.93	4.95	4.97	4.96	4.94	5.22	5.28
Mn4-Ca	A	3.83	3.79	3.83	3.82	3.99	4.10	4.07	4.05	4.01	4.06	4.11	4.12	4.12	4.09
	B	3.76	3.84	3.83	3.88	3.93	4.10	4.06	3.97	3.93	3.99	4.10	4.01	4.06	4.03
	Ave.	3.80	3.82	3.83	3.85	3.96	4.10	4.07	4.01	3.97	4.03	4.11	4.07	4.09	4.06
Yz-D1-H190	A	2.50	2.54	2.82	2.85	2.61	2.51	2.47	2.52	2.53	2.57	2.63	2.70	2.58	2.58
	B	2.51	2.67	2.78	2.80	2.71	2.54	2.54	2.58	2.58	2.58	2.56	2.70	2.63	2.56
	Ave.	2.51	2.61	2.80	2.83	2.66	2.53	2.51	2.55	2.56	2.58	2.60	2.70	2.61	2.57
Ca-D1-E189	A	2.98	3.03	3.05	3.04	2.94	2.88	2.85	2.89	2.90	2.91	2.92	2.99	3.09	3.10
	B	3.03	3.03	3.01	3.00	2.95	2.91	2.86	2.89	2.93	2.95	2.93	2.97	3.03	3.08
	Ave.	3.01	3.03	3.03	3.02	2.95	2.90	2.86	2.89	2.92	2.93	2.93	2.98	3.06	3.09
D1-E65-D2-E312	A	2.53	2.64	2.61	2.59	2.61	2.56	2.62	2.56	2.68	2.59	2.66	2.58	2.60	2.66
	B	2.54	2.57	2.59	2.55	2.60	2.62	2.58	2.61	2.59	2.60	2.58	2.59	2.61	2.58
	Ave.	2.54	2.61	2.60	2.57	2.61	2.59	2.60	2.59	2.64	2.60	2.62	2.59	2.61	2.62
D1-E65-D1-R334	A	3.00	3.05	3.10	2.96	3.09	3.10	3.11	2.99	3.07	3.00	2.99	2.93	3.16	3.06
	B	2.93	2.84	2.80	2.93	2.85	2.88	3.03	2.96	2.95	2.79	2.91	2.94	2.85	2.87
	Ave.	2.97	2.95	2.95	2.95	2.97	2.99	3.07	2.98	3.01	2.90	2.95	2.94	3.01	2.97
D2-E312-D1-R334	A	3.06	3.06	2.96	2.91	2.96	2.98	3.05	2.99	2.97	2.91	2.94	3.07	2.90	3.02
	B	3.11	3.05	3.09	3.05	3.02	3.00	3.12	3.11	3.02	3.01	2.89	3.02	3.05	3.03
	Ave.	3.09	3.06	3.03	2.98	2.99	2.99	3.09	3.05	3.00	2.96	2.92	3.05	2.98	3.03

Reporting Summary

Nature Portfolio wishes to improve the reproducibility of the work that we publish. This form provides structure for consistency and transparency in reporting. For further information on Nature Portfolio policies, see our [Editorial Policies](#) and the [Editorial Policy Checklist](#).

Statistics

For all statistical analyses, confirm that the following items are present in the figure legend, table legend, main text, or Methods section.

- | | |
|-------------------------------------|--|
| n/a | Confirmed |
| <input type="checkbox"/> | <input checked="" type="checkbox"/> The exact sample size (n) for each experimental group/condition, given as a discrete number and unit of measurement |
| <input checked="" type="checkbox"/> | <input type="checkbox"/> A statement on whether measurements were taken from distinct samples or whether the same sample was measured repeatedly |
| <input checked="" type="checkbox"/> | <input type="checkbox"/> The statistical test(s) used AND whether they are one- or two-sided
<i>Only common tests should be described solely by name; describe more complex techniques in the Methods section.</i> |
| <input checked="" type="checkbox"/> | <input type="checkbox"/> A description of all covariates tested |
| <input checked="" type="checkbox"/> | <input type="checkbox"/> A description of any assumptions or corrections, such as tests of normality and adjustment for multiple comparisons |
| <input type="checkbox"/> | <input checked="" type="checkbox"/> A full description of the statistical parameters including central tendency (e.g. means) or other basic estimates (e.g. regression coefficient) AND variation (e.g. standard deviation) or associated estimates of uncertainty (e.g. confidence intervals) |
| <input checked="" type="checkbox"/> | <input type="checkbox"/> For null hypothesis testing, the test statistic (e.g. F , t , r) with confidence intervals, effect sizes, degrees of freedom and P value noted
<i>Give P values as exact values whenever suitable.</i> |
| <input checked="" type="checkbox"/> | <input type="checkbox"/> For Bayesian analysis, information on the choice of priors and Markov chain Monte Carlo settings |
| <input checked="" type="checkbox"/> | <input type="checkbox"/> For hierarchical and complex designs, identification of the appropriate level for tests and full reporting of outcomes |
| <input checked="" type="checkbox"/> | <input type="checkbox"/> Estimates of effect sizes (e.g. Cohen's d , Pearson's r), indicating how they were calculated |

Our web collection on [statistics for biologists](#) contains articles on many of the points above.

Software and code

Policy information about [availability of computer code](#)

Data collection

Data analysis

For manuscripts utilizing custom algorithms or software that are central to the research but not yet described in published literature, software must be made available to editors and reviewers. We strongly encourage code deposition in a community repository (e.g. GitHub). See the Nature Portfolio [guidelines for submitting code & software](#) for further information.

Data

Policy information about [availability of data](#)

All manuscripts must include a [data availability statement](#). This statement should provide the following information, where applicable:

- Accession codes, unique identifiers, or web links for publicly available datasets
- A description of any restrictions on data availability
- For clinical datasets or third party data, please ensure that the statement adheres to our [policy](#)

The atomic coordinates and structure factors have been deposited in the Protein Data Bank under the following IDs: 8IR5 for OF (dark, ground state for the Δt_1 structures), 8IR6 for $\Delta t_1 = 20$ ns, 8IR7 for $\Delta t_1 = 200$ ns, 8IR8 for $\Delta t_1 = 1$ μ s, 8IR9 for $\Delta t_1 = 30$ μ s, 8IRA for $\Delta t_1 = 200$ μ s, 8IRB for $\Delta t_1 = 5$ ms, 8IRC for 1F (ground state)

(for the Δt_2 structures), 8IRD for $\Delta t_2 = 20$ ns, 8IRE for $\Delta t_2 = 200$ ns, 8IRF for $\Delta t_2 = 1$ μ s, 8IRG for $\Delta t_2 = 30$ μ s, 8IRH for $\Delta t_2 = 200$ μ s, and 8IRI for $\Delta t_2 = 5$ ms. All other data with a PDB code used in this study are adopted from the PDB databank.

Research involving human participants, their data, or biological material

Policy information about studies with [human participants or human data](#). See also policy information about [sex, gender \(identity/presentation\), and sexual orientation](#) and [race, ethnicity and racism](#).

Reporting on sex and gender	n/a
Reporting on race, ethnicity, or other socially relevant groupings	n/a
Population characteristics	n/a
Recruitment	n/a
Ethics oversight	n/a

Note that full information on the approval of the study protocol must also be provided in the manuscript.

Field-specific reporting

Please select the one below that is the best fit for your research. If you are not sure, read the appropriate sections before making your selection.

Life sciences Behavioural & social sciences Ecological, evolutionary & environmental sciences

For a reference copy of the document with all sections, see nature.com/documents/nr-reporting-summary-flat.pdf

Life sciences study design

All studies must disclose on these points even when the disclosure is negative.

Sample size	The sample size is determined based on the number of diffraction images that produced reasonably high resolution and multiplicity or number of unique diffractions in each time-resolved serial crystallography data set. The microcrystals obtained were reproducible, and the diffraction data was processed with standard crystallographic software (Methods section), which resulted in standard data statistics as shown in Extended Data Table 1.
Data exclusions	No data was excluded; for details of the data analysis statistics, see Extended Data Table 1.
Replication	Thousands of microcrystals were used to obtain a full diffraction dataset, which showed that the results are well reproduced. The repetition rate of a specific dataset was shown in Extended Data Table 1, in which, it was shown that the repetition rate is over 100 even for the highest resolution shell for each of the dataset.
Randomization	The microcrystals used for the diffraction experiments were not chosen, and diffraction data from good microcrystals were used for the structural analysis. The criterion for choosing good diffraction data is based on the resolution as well as their deviations from standard cell parameters, as described in the Methods section.
Blinding	Not applicable. All experimental maps were included in the statistical analysis.

Reporting for specific materials, systems and methods

We require information from authors about some types of materials, experimental systems and methods used in many studies. Here, indicate whether each material, system or method listed is relevant to your study. If you are not sure if a list item applies to your research, read the appropriate section before selecting a response.

Materials & experimental systems

- n/a Involved in the study
- Antibodies
 - Eukaryotic cell lines
 - Palaeontology and archaeology
 - Animals and other organisms
 - Clinical data
 - Dual use research of concern
 - Plants

Methods

- n/a Involved in the study
- ChIP-seq
 - Flow cytometry
 - MRI-based neuroimaging

Plants

Seed stocks

n/a

Novel plant genotypes

n/a

Authentication

n/a